

# **Reconciling Lithospheric Rheology Between Laboratory Experiments, Field Observations, and Different Tectonic Settings**

\*Ashley Bellas<sup>1</sup>, Shijie Zhong<sup>1</sup>, and Anthony B. Watts<sup>2</sup>

[\\*ashley.bellas@colorado.edu](mailto:ashley.bellas@colorado.edu)

[shijie.zhong@colorado.edu](mailto:shijie.zhong@colorado.edu)

[tony.watts@earth.ox.ac.uk](mailto:tony.watts@earth.ox.ac.uk)

Department of Physics, University of Colorado, Boulder<sup>1</sup>

Department of Earth Sciences, University of Oxford<sup>2</sup>

## **Abstract**

Recent modeling studies have shown that laboratory-derived rheology is too strong to reproduce observations of flexure at the Hawaiian Islands, while the same rheology appears consistent with outer rise – trench flexure at circum-Pacific subduction zones. Collectively, these results indicate that the rheology of an oceanic plate boundary is stronger than that of its interior, which, if correct, presents a challenge to understanding the formation of trenches and subduction initiation. To understand this dilemma, we first investigate laboratory-derived rheology using fully dynamic viscoelastic loading models and find that it is too strong to reproduce the observationally inferred elastic thickness,  $T_e$ , at most plate interior settings. The  $T_e$  can, however, be explained if the yield stress of low-temperature plasticity is significantly reduced, for example, by reducing the activation energy from 320 kJ/mol, as in Mei et al. (2010), to 190 kJ/mol as was required by previous studies of the Hawaiian Islands, implying that the lithosphere beneath Hawaii is not anomalous. Second, we test the accuracy of the modeling methods used to constrain the rheology of subducting lithosphere, including the Yield Stress Envelope (YSE) method, and the Broken Elastic Plate Model (BEPM). We show the YSE method accurately reproduces the model  $T_e$  to within ~10% error with only modest sensitivity to the assumed strain rate and curvature. Finally, we show that the response of a continuous plate is significantly enhanced when a free edge is introduced at or near an edge load, as in the BEPM, and is sensitive to the degree of viscous coupling at the free edge. Since subducting lithosphere is continuous and generally mechanically coupled to a sinking slab, the BEPM may falsely introduce a weakness and hence overestimate  $T_e$  at a trench because of tradeoff. This could explain the results of recent modeling studies that suggest the rheology of subducting oceanic

23 plate is stronger than that of its interior. However, further studies using more advanced thermal  
24 and mechanical models will be required in the future in order to quantify this.

25 **Key words**

26 Rheology: crust and lithosphere; Lithospheric flexure; Mechanics, theory, and modelling.

## **1. Introduction**

Plate tectonics implies that the plates behave rigidly in the way they respond to loads on long geological time-scales. The principal evidence for a rigid oceanic lithosphere has come from observations of flexure which show that the effective elastic thickness,  $T_e$ , (equivalent to flexural rigidity) increases with age away from a mid-ocean ridge (Watts, 1978) and from experimental rock mechanics data which suggest that while its strength is limited by brittle deformation in its upper part and ductile flow in its lower part, the lithosphere has an intervening elastic ‘core’ that increases in thickness with age (Goetze & Evans, 1979; Watts & Burov, 2003). Recent studies based on modeling plate flexure (Hunter & Watts (2016) for circum-Pacific trench – outer rise systems and Zhong & Watts (2013) for Hawaiian Islands) and low-temperature plasticity laws (e.g., Mei et al. 2010) suggest, however, spatial variations in plate rigidity, with subduction zones appearing stronger than expected for the age of the plate at the time of loading and the interior of plates weaker. This poses a dilemma, especially for the formation of deep-sea trenches and the initiation of subduction, since plate boundaries would be expected to be generally weaker, not stronger, than plate interiors.

Possible explanations for this dilemma include consideration of the time-scales of loading (Hunter & Watts, 2016), the role of flexure-induced bending stresses (Craig et al, 2014) and faulting (Billen & Gurnis, 2005) and the thermal effects of magma-assisted flexure (Buck et al., 2015) due, for example, to ‘petit’ spots (Hirano et al. 2008) or deep mantle plumes (Pleus et al., 2020). Hunter and Watts (2016), for example, found that while there is indeed evidence of a localized weak zone in the region of the seaward wall of a trench where the curvature of flexure is highest, the ‘background’  $T_e$  of a trench – outer rise system (their so-called ‘seaward  $T_e$ ’) was controlled by a relatively high (671-714° C) oceanic isotherm compared to that found at the

Hawaiian Islands ( $\sim 450^\circ \text{C}$ ). Similarly, McNutt (1984) found the mechanical thickness of subducting lithosphere to generally be larger than that at ocean island settings, and attributed the difference to regional thermal anomalies. However, there is increasing evidence to suggest that thermal rejuvenation by the Hawaiian plume does not significantly modify the lithospheric thermal structure (Ribe & Christensen, 1994), surface heat flux (von Herzen, 1989), nor does it support swell topography which appears to be dynamic (e.g., Ribe & Christensen, 1994; Zhong & Watts, 2002; Cadot et al., 2012; Huppert et al., 2020). Therefore, that estimates of  $T_e$  from recent studies indicate lithospheric rheology is stronger (i.e., higher yield stress) at subduction zones than at ocean island settings is not easily understood.

The purpose of this paper is to address this dilemma by reevaluating some of the methods that have been used to model plate flexure and their implications for understanding the rheology of oceanic lithosphere in plate boundary and interior settings. Our focus is on the validity of Broken Elastic Plate Models (BEPM) and the Yield Strength Envelope (YSE) methods used to estimate  $T_e$ , the sensitivity of these estimates to some of the parameters in laboratory-derived rheological laws, and the effects of regional variations in the thermal and/or magmatic structure on  $T_e$ . We use fully dynamic viscoelastic loading models to show that the YSE method accurately reproduces  $T_e$  and the state of stress of flexed oceanic lithosphere, and that the BEPM method significantly enhances the flexure such that a tradeoff exists and an oceanic plate may appear stronger than it actually is, and that  $T_e$  at a majority of seamount and ocean-islands is overestimated by a factor of approximately two by laboratory-derived rheology.

## **2. Models and Methods**

In this section, we present lithospheric rheology including brittle and ductile yielding mechanisms. We then introduce the YSE method and the numerical viscoelastic loading model.

73 The elastic plate model (EPM) and BEPM are well documented in previous studies and so are  
 74 reproduced here only visually (Figure 1) (for full details, refer to Turcotte & Schubert, 1982, or  
 75 Watts, 2001). The lithosphere may be approximated to first order as an elastic plate, but more  
 76 complete models include the possibility for anelastic yielding that may occur under high stress  
 77 and high temperature conditions.

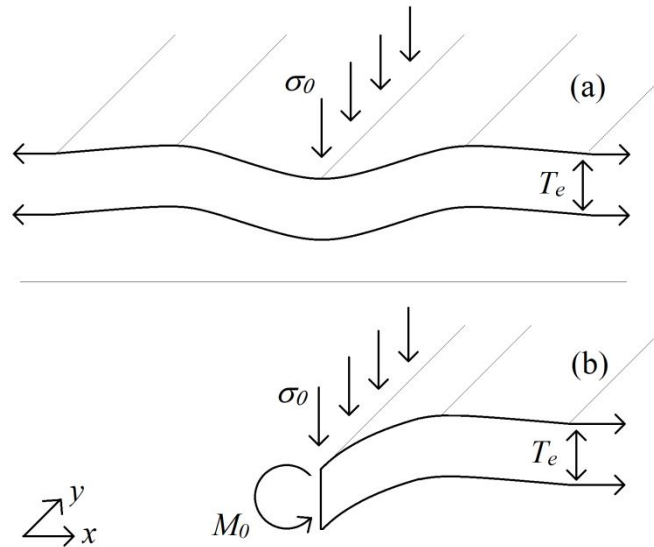


**Figure 1. Schematics of the Elastic Plate Model and the Broken Elastic Plate Model.** (a) The EPM is infinite in 2D space. The plate is assumed to be thin relative to the width or wavelength of the load such that vertical variations within the plate can be neglected. The load pictured is an infinite line load or delta function in  $x$ , and constant in  $y$ . Commonly used loads also include sinusoidal loads and finite-width loads. (b) The BEPM is identical to the EPM except that the model geometry is semi-infinite in  $x$  and a bending moment is often applied to the free edge. The deformational response in both the EPM and the BEPM is purely elastic.

## 2.1 Lithospheric Rheology

Laboratory studies suggest that when stress exceeds the local elastic limit, anelastic yielding of the lithosphere is controlled by (i) frictional sliding, (ii) low-temperature plasticity (also commonly referred to as dislocation glide or Peierls creep), and (iii) high-temperature creep. The yield stress of frictional sliding is formulated (Byerlee, 1978)

$$\tau_{yield} = \mu_f \rho g z, \#(1)$$

in which  $\mu_f$  is the frictional coefficient of a pre-existing fault,  $\rho$  is density,  $g$  acceleration due to gravity, and  $z$  is depth. This simple formulation assumes that the normal stress on an arbitrary fault is equal to the local lithostatic pressure, although it is also straightforward to consider the differing normal stress and strength of normal, reverse, and strike-slip faults. While the seminal laboratory study of Byerlee (1978) estimated the frictional coefficient  $\mu_f=0.7$ , observational and modeling studies estimate  $\mu_f=0.3$  based on the dip angle newly formed faults in the outer-rise at subduction zones (Craig et al., 2014), as well as based on the seismic strain rate at the Hawaiian Islands (Bellas & Zhong, 2021). Based on observations of heat flux above interplate thrust faults,  $\mu_f < 0.1$  (Gao & Wang, 2014; England, 2018). The reasons for this spread in  $\mu_f$  between different tectonic settings and laboratory conditions are not generally understood.

Low-temperature plasticity (i.e., dislocation glide or Peierls creep) is formulated (e.g., Mei et al., 2010)

$$\dot{\epsilon} = A \sigma^n \exp \left( - \frac{E_p}{RT} \left( 1 - \left( \frac{\sigma}{\sigma_p} \right)^p \right)^q \right), \#(2)$$

in which  $\dot{\epsilon}$  and  $\sigma$  are the 2<sup>nd</sup> invariants of the strain rate and deviatoric stress tensors, respectively,  $A$  is the pre-exponential factor,  $n$  is a constant,  $E_p$  is the plastic activation energy,  $R$  is the gas constant,  $T$  is temperature,  $\sigma_p$  is the Peierls stress, and  $p$  and  $q$  are constants

determined in experiments (Figure 2a,b). Different laboratory studies estimate significantly different parameter values which may be resolved by considering the length scales of deformation (Kumamoto et al., 2017). However, even the weakest of laboratory-derived low-temperature plasticity flow laws (Idrissi et al., 2016) is too strong to reproduce observations of flexure at the Hawaiian Islands (Zhong & Watts, 2013; Bellas et al., 2020). Zhong & Watts (2013) showed that the flexural strength of the lithosphere is controlled to first order by low-temperature plasticity, and so this deformation mechanism is of greatest importance in the following work.

High-temperature creep including diffusion and dislocation creep may be formulated as a composite law (e.g., Podolefsky et al., 2004; Zhong & Watts, 2013)

$$\dot{\epsilon} = B\sigma(\sigma_T^{m-1} + \sigma^{m-1})\exp\left(-\frac{E_c}{RT} + \frac{E_c}{RT_m}\right), \#(3)$$

in which  $B$  is a pre-exponential factor,  $\sigma_T$  is the transition stress at which diffusion and dislocation creep contribute equally to strain rate,  $m$  is a constant,  $E_c$  is the high-temperature creep activation energy which we assume to be equal for diffusion and dislocation creep for simplicity, and  $T_m$  is the reference mantle temperature. The parameter values for high-temperature creep used in this study reproduce observations of seismic anisotropy in geodynamic models (Podolefsky et al., 2004) (Table 1). High-temperature creep is generally well-understood from laboratory studies (Karato & Wu, 1993; Hirth & Kohlstedt, 2003), studies of the long-wavelength geoid (e.g., Hager & Richards, 1989), post-glacial rebound (e.g., Mitrovica & Forte, 1997), and post-seismic deformation (e.g., Freed et al., 2010), and does not have a strong influence on flexure (Zhong & Watts, 2013).



121        In Figure 2a, we show the yield stress envelope defined by these three deformation  
122 mechanisms. Macroscopic yielding occurs when stress exceeds the local yield stress, while stress  
123 below the local yield stress causes elastic deformation (Figure 2b). The yield stress associated  
124 with each deformation mechanism is solved from constitutive equations (1-3) by assuming either  
125 a strain rate and a temperature profile (low-temperature plasticity and high-temperature creep) or  
126 increasing lithostatic pressure with depth (frictional sliding).

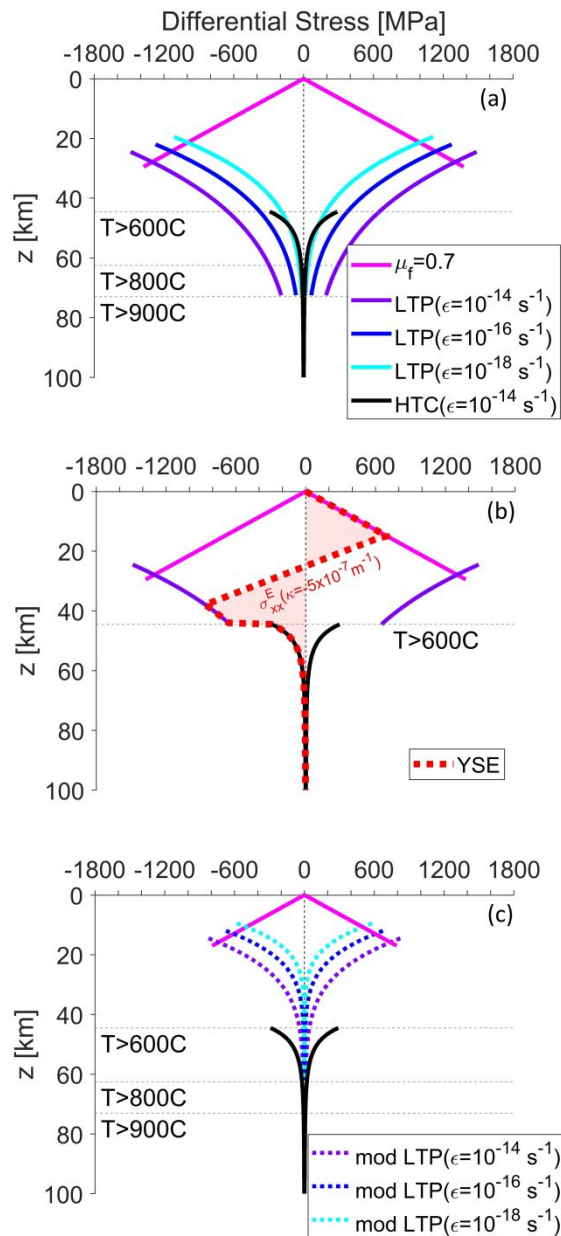


**Figure 2. Lithospheric rheology and the Yield Stress Envelope (YSE).** The yield stress envelope represents lithospheric strength as a function of depth in terms of the maximum stress,  $\sigma_{xx}$ , that can be supported at each depth. A 90 Ma thermal structure is assumed in all panels based on the half-space cooling model. (a) The yield stress envelope based on laboratory-derived rheology for frictional sliding ( $\mu_f$ ), low-temperature plasticity (LTP) and high-temperature creep (HTC). (b) Same as (a), except the intersection of elastic bending stresses (dashed red) with the yield stress envelope is shown. (c) Same as (a), except the activation energy of low-temperature plasticity is reduced from 320 kJ/mol to 190 kJ/mol as is required to reproduce observations of flexure at the Hawaiian Islands (Zhong & Watts, 2013; Bellas et al., 2020).

127 **Table 1. Model Parameters**

Parameter	Value
Shear modulus, $\mu$	$3.3333 \times 10^{10}$ Pa
Reference viscosity, $\eta_0$	$10^{20}$ Pa s
Gravitational acceleration, $g$	$10$ m/s <sup>2</sup>
Gas constant, $R$	$8.32$ J/(mol K)
Mantle density, $\rho$	$3330$ kg/m <sup>3</sup>
Mantle Temperature, $T_m$	$1350$ °C

*Frictional sliding (Byerlee, 1978)*

$$\eta = \frac{\sigma}{2\dot{\epsilon}} = \frac{\tau_{yield}}{\dot{\epsilon}} = \frac{\mu_f \sigma_n}{\dot{\epsilon}}$$

\*Frictional coefficient,  $\mu_f$  0.7

*Low-temperature plasticity (Mei et al., 2010)*

$$\eta = \frac{\sigma}{2\dot{\epsilon}} = \frac{\sigma^{1-n}}{A} \exp \left\{ \frac{E_p}{RT} \left[ 1 - \left( \frac{\sigma}{\sigma_p} \right)^p \right]^q \right\}$$

Pre-exponential factor,  $A$   $1.4 \times 10^{-7}$  MPa<sup>-2</sup>

\*Activation energy,  $E_p$  320 kJ/mol

Peierls stress,  $\sigma_p$  5.9 GPa

Stress exponent,  $n$  2

Stress exponent,  $p$  1/2

Stress exponent,  $q$  2

*High-temperature creep (Podolefsky et al., 2004)*

$$\eta = \frac{\sigma}{2\dot{\epsilon}} = \frac{\eta_0}{1 + (\sigma/\sigma_T)^{m-1}} \exp \left( \frac{E_c}{RT} - \frac{E_c}{RT_m} \right)$$

Stress exponent,  $m$  3.5

Transition stress,  $\sigma_T$   $3 \times 10^5$  Pa

Activation energy,  $E_c$  360 kJ/mol

\*Activation temperature,  $T_{HTC}$  800 °C

\*Parameters marked with an asterisk are varied to test their influence on flexure (Table 2). Note that although the reference viscosity is  $10^{20}$  Pa s, a minimum viscosity of  $10^{21}$  Pa s is imposed in numerical models.

## 2.2 The Yield Stress Envelope Method

The YSE method asserts that the effective elastic thickness,  $T_e$ , of a yielding plate can be defined based on the bending moment at a given curvature (McNutt & Menard, 1982). The bending moment of a yielding plate can be calculated from the general expression of the bending moment,

$$M_0 = \int \sigma_{xx}(z - z_n) dz, \#(4)$$

in which  $\sigma_{xx}$  is the differential stress due to flexure,  $z$  is depth, and  $z_n$  is depth to the neutral plane in the flexed plate. Note that the differential stress in a yielding plate is given by the elastic bending stress truncated by the YSE, where the elastic bending stress is expressed

$$\sigma_{xx} = \frac{\kappa E(z - z_n)}{1 - \nu^2}, \#(5)$$

in which  $\kappa$  is curvature,  $E$  is Young's modulus, and  $\nu$  is Poisson's ratio. Note also that the total stress component  $\sigma_{zz}=0$  such that differential stress is given by  $\sigma_{xx}$ .

The intersection of the elastic bending stress with the YSE (i.e., the integrand in equation 4) is presented in Figure 2b. To solve  $T_e$  of a yielding plate, the bending moment of the yielding plate (equation 4, Figure 2b) is equated to the bending moment of a purely elastic plate, which is expressed

$$M_0 = \frac{\kappa E}{12(1 - \nu^2)} T_e^3, \#(6)$$

It is worth noting here that the YSE method is generally applied with numerous approximations and simplifications. For example, the YSE is typically solved for a constant values of strain rate, curvature, neutral plane depth, although they may vary significantly in time and space. Previous work has shown that the YSE method is most accurate when the maximum curvature is chosen

(Mueller & Phillips, 1994), but we will perform a test of this method against fully dynamic models for the first time here.

### 2.3 The Viscoelastic Loading Model

Viscoelastic loading models are fully dynamic, meaning they account for spatial and temporal variations in stress, strain rate, curvature, etc. Comparing the fully dynamic solutions with those of the YSE method will allow us to test whether these spatial variations are necessary to resolve for an accurate estimate of elastic thickness. We will also use the viscoelastic loading model to investigate the efficacy of applying the BEPM to model flexure at subduction zones.

Deformation of an incompressible viscoelastic medium is expressed by the conservation equations of mass and momentum (e.g., Zhong & Watts, 2013)

$$u_{i,i} = 0, \#(7)$$

$$\sigma_{ij,j} - (\rho g u_3)_{,i} = 0, \#(8)$$

in which  $u_i$  is the displacement,  $\sigma_{ij}$  is the stress tensor,  $\rho$  density,  $g$  acceleration due to gravity, and subscripts after a comma denote a spatial derivative. The constitutive equation of a Maxwellian medium is

$$\sigma_{ij} + \frac{\eta}{\mu} \dot{\sigma}_{ij} = -p\delta_{ij} - 2\eta\dot{\epsilon}_{ij}, \#(9)$$

in which  $\eta$  is the viscosity,  $\mu$  the shear modulus,  $\dot{\sigma}_{ij}$  the stress rate tensor,  $p$  pressure, and  $\dot{\epsilon}_{ij}$  the strain rate tensor. Maxwellian rheology represents viscous and elastic deformation combined in series (e.g., Zhong et al., 2003). An important timescale for viscoelastic deformation is given by the Maxwell time,  $\tau_M = \eta/\mu$  (e.g.,  $\sim 950$  years for  $\eta = 10^{21}$  Pa s), which is the characteristic timescale on which viscoelastic deformation occurs.

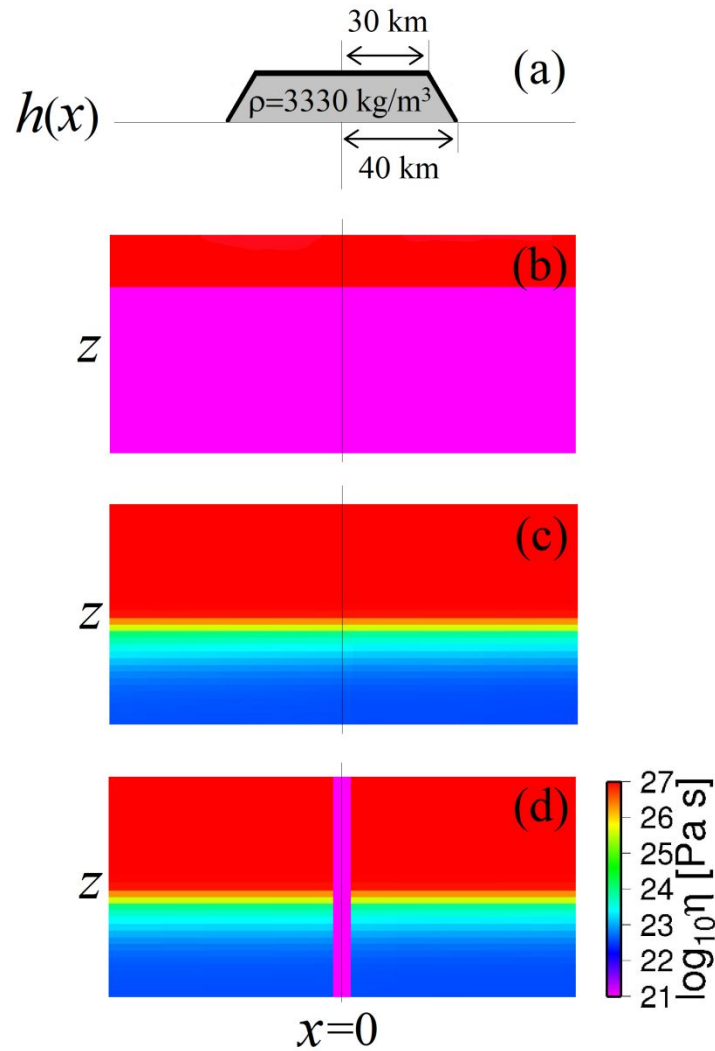


**Figure 3. Schematic of viscoelastic loading models.** We present the load and examples of the three main viscosity structures that are assigned in 2D viscoelastic loading models (not to scale). (a) The load is applied to the surface boundary as a normal stress related to topography following  $\sigma_0 = \rho gh(x)$ . Viscoelastic loading models are configured either with two-layer viscosity (b), with viscosity based on laboratory studies (c), or with viscosity based on laboratory studies and an imposed weak zone of finite width centered on  $x=0$  (d). The shear modulus throughout the domain is uniform. Note that the models are configured with a reflecting boundary condition at  $x=0$ . In all other figures, only results on the right-hand side of  $x=0$  are presented, across which results are symmetric.

In the numerical models, the viscosity field is defined in one of three major ways to emulate and test the YSE method and BEPM. First, and most simply, viscosity may be bimodal with two vertically stratified layers (e.g., Figure 3b). In two-layer models, a high viscosity plate ( $10^{27}$  Pa s) overlies a low viscosity mantle ( $10^{21}$  Pa s). This two-layer viscosity structure simulates an elastic plate with thickness equal to that of the high viscosity plate because essentially zero viscous stress relaxation occurs in the high-viscosity layer on the timescales relevant to flexure. Therefore, the high-viscosity plate is effectively a purely elastic plate, and this has been demonstrated in benchmark calculations with the EPM in previous work (e.g., Zhong, 1997; Zhong & Watts, 2013).

Second, viscosity may be defined based on the laboratory-derived constitutive equations (1-3) and the relationship  $\eta = \sigma / 2\dot{\epsilon}$  to test the YSE method (Figure 3c). In the models, viscosity is defined by high-temperature creep (equation 3) wherever temperature exceeds an imposed activation temperature,  $T_{HTC}$ . The activation temperature is varied from 600 °C to 900 °C in our study, a range which is approximately centered on the value recommended by laboratory studies of 800 °C (Mei et al., 2010). It is important to impose  $T_{HTC}$  because high-temperature creep is limited by diffusional processes on the microscale, which are activated by thermal energy. In particular, diffusion creep is limited by diffusion of grain boundaries, and dislocation creep is limited by the diffusion of dislocations and/or crystallographic defects (i.e., the climb velocity of jogs) (Karato, 2012; Mei et al., 2010). Wherever temperature is less than  $T_{HTC}$ , the viscosity is defined by the lower of those predicted by frictional sliding and low-temperature plasticity (e.g., Figure 3c).

Third, viscosity may be defined based on laboratory-derived constitutive equations (1-3) and with a low-viscosity zone imposed near  $x=0$  to test the BEPM (e.g., Figure 3d). Imposing

such a weak zone allows us to simulate a free edge, because the lithospheric plate is effectively free and decoupled near  $x=0$ . We aim to configure a fully dynamic model with effectively semi-infinite geometry and a free edge as in the BEPM to test the implications of the BEPM when it is applied to model flexure at subduction zones.

The key motivation behind the numerical model setups is to estimate the effective elastic thickness,  $T_e$ , of a complex viscosity lithosphere. To estimate  $T_e$ , we compare the steady-state flexure from a complex viscosity model with many two-layer models for which the high-viscosity layer thickness ( $T_e$ ) is varied in 1 km increments. Then, the  $T_e$  of the complex viscosity model is given by the two-layer model which best-reproduces the steady-state flexure. This methodology accounts for spatial variations in strain rate, stress, curvature etc., which will allow us to test whether simplified methods such as the YSE and BEPM accurately account for these variations based on their estimates of  $T_e$ . In addition, since the numerical models are used only to estimate  $T_e$  and we do not compare predictions with observed flexural profiles, we are afforded several simplifications. In particular,  $T_e$  is either completely insensitive or weakly sensitive to the load for linear and nonlinear rheology, respectively (refer to Results section 3.1), and we neglect infill of the flexural depression by sediment or rocks and the weight of water, although results are not appreciably changed compared to previous work which included these effects (e.g., Bellas et al., 2020).

We assume a load that is constant in time and imposed as a normal stress on the surface boundary (Figure 3a). The load is trapezoidal in shape with bottom-half-width equal to 40 km, top-half-width equal to 30 km, height equal to 3 km or 6 km, and the normal stress corresponds to local topography and mantle density following  $\sigma_0=\rho gh(x)$ , where  $h(x)$  is the topography of the load (Figure 3, Table 2). Since the load is imposed as a normal stress on the surface and the



weight of water is neglected, a surface load with 3 km height and mantle density corresponds to a load of 5.3 km height and 2900 kg/m<sup>3</sup> density (i.e., that of intrusive mafic rocks) (Watts et al., 2021) when the weight of water is considered. Similarly, a load with 6 km height in our simplified models corresponds to a seamount with 10.6 km height, and we suggest that these load choices adequately represent the observed spread in seamount heights around the globe.

The governing equations are solved using a finite element model, CitcomSVE, that was originally developed for modeling glacial isostatic adjustment in a spherical shell geometry (Zhong et al., 2003) and later modified to include nonlinear rheology and Cartesian geometry (Zhong & Watts, 2013). All numerical models in this study have 2D Cartesian geometry, uniform mantle density, and uniform elastic properties. The vertical sidewall and bottom boundary conditions are free-slip (i.e., reflecting), and the surface boundary is a free and deformable surface (i.e., stress-free). The reflecting boundary conditions allow models to simulate loading in a domain that is effectively infinite in the horizontal dimension. The model domain is 1500 km wide ( $x$ ), and 600 km deep ( $z$ ) with 256 horizontal elements and 160 vertical elements. Horizontal grid refinement is applied near the load, such that the horizontal resolution is 2 km at  $x=0$  km and increases linearly to 10 km at  $x=1500$  km. The vertical resolution is 2.5 km in the upper 100 km and 4.2 km in the lower 500 km in all complex viscosity models. In two-layer viscosity models, the vertical resolution is 3-4 km in the high-viscosity layer. Numerical models are evolved in time with time-steps equal to a quarter Maxwell time,  $\tau_M/4 \sim 238$  years. Note that all model results are symmetric across  $x=0$ . All parameter values and cases are additionally summarized in Tables 1-3.

**3. Results**

Results are presented in three major sections. First, in section 3.1, we predict  $T_e$  based on laboratory-derived rheology for a broad range of parameter values and compare predictions with observations. Second, in section 3.2, we test whether the YSE method accurately reproduces the  $T_e$  of fully dynamic viscoelastic loading models. Third, in section 3.3, we investigate the effects of introducing a free edge in models of flexure as is done in the BEPM. Finally, in the Appendix, interested readers will find an analysis of the type of error that arises in the classic EPM when the thin plate approximation breaks down.

### 3.1 Laboratory-Derived Lithospheric Rheology and Global Observations of Flexure

It has been suggested that the Hawaiian lithosphere may be weaker than laboratory-derived rheology would predict (Zhong & Watts, 2013; Hunter & Watts, 2016; Bellas et al., 2020) because it is thermomechanically eroded by the Hawaiian plume (e.g., Hunter & Watts, 2016; Pleus et al., 2020), and/or due to magmatic diking and intrusion (Buck et al., 2015). Hypothetically, if the discrepancy between the observed and predicted flexure at the Hawaiian Islands is indeed caused by thermal and/or magmatic anomalies, then we expect that laboratory-derived lithospheric rheology would more accurately reproduce flexure elsewhere, for example, at ocean-island settings where plume activity and volcanism are not as extensive such as Bermuda, Cape Verde, the Island of Mayotte, or the Canary Islands. We would consider it highly unlikely for mantle plumes, magmatic diking and intrusion to modify the lithosphere to equal degree at many seamounts and ocean islands with much weaker plume activity and volcanism than that at the Hawaiian Islands. In contrast, if the source of the discrepancy is that laboratory-derived rheology is too strong, then laboratory-derived rheology should repeatedly underestimate flexure at many ocean island settings to approximately equal degree no matter the extent of plume activity and volcanism. To discriminate between these possibilities, we formulate

261 viscoelastic loading models with a broad range of lithospheric thermal ages and load amplitudes  
262 (e.g., Figure 4) and compare with a global observational dataset of elastic thickness,  $T_e$  (Figure 5).

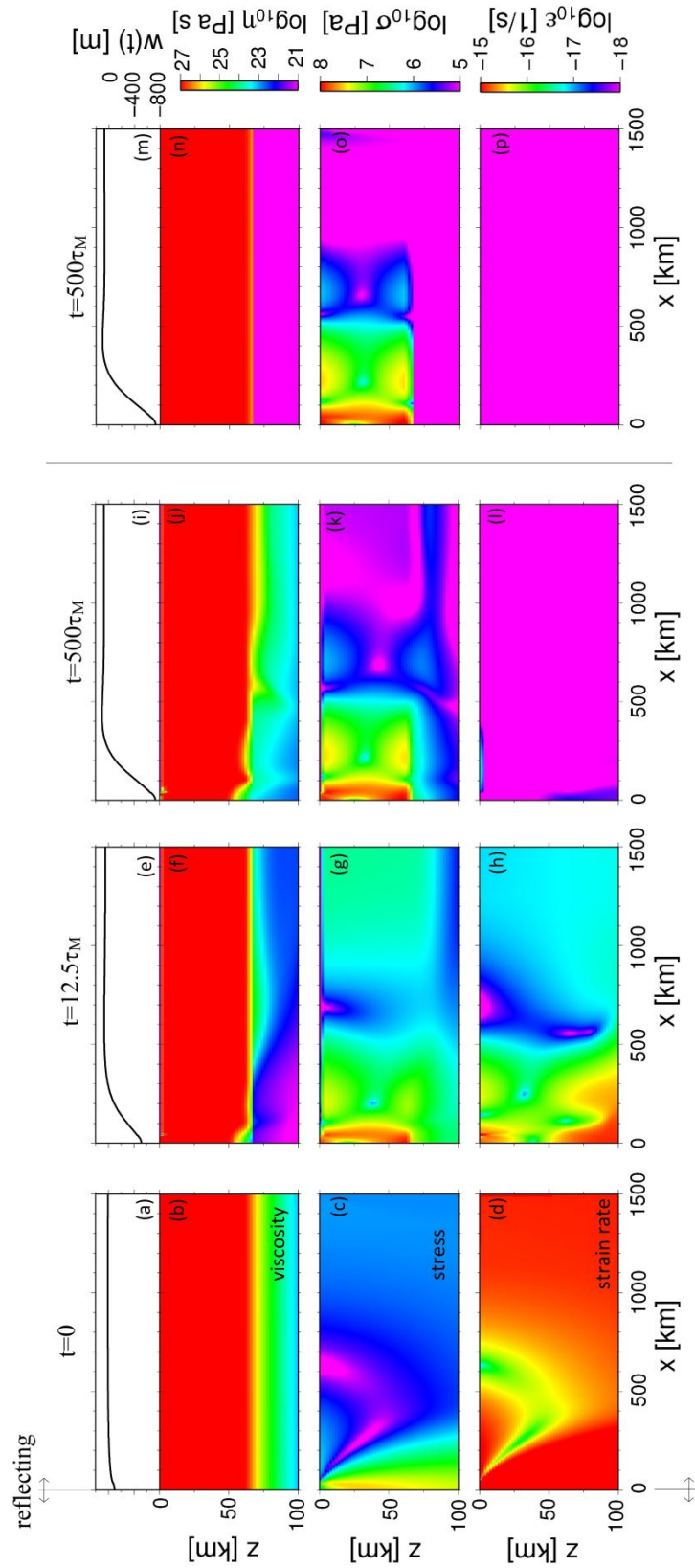


**Figure 4. Time evolution of Case 1h and a snapshot of the best-fit two-layer model.** Note that only half of the flexural profile or field is pictured here (results are reflected across  $x=0$ ), and only the upper 100 km of the domain is shown, though it is 600 km deep. At  $t=0$  (a-d), the response of the system is purely elastic. When time has reached  $t=12.5\tau_M$  (e-h), viscous relaxation has caused stress to concentrate in the lithosphere near the load, and strain to concentrate in the shallow lithosphere and weak underlying mantle near the load. When time has reached  $t=500\tau_M$  (i-l), the system has reached steady state. The best-fit to steady-state flexure is produced by a two-layer model with  $T_e=64$  km (m-p).

264 In the viscoelastic loading models, lithospheric thermal age is varied from 20 Ma to 130 Ma  
 265 in 10 Ma increments, and the thermal structure is calculated using the half-space cooling model.  
 266 The time-dependent flexural response to the load is computed for 500 Maxwell times to a steady-  
 267 state ( $\sim 475$  kyr,  $\tau_M = \eta_0/\mu$ ). In Case 1h, which belongs to Suite 1, the thermal age is 90 Ma, the  
 268 frictional coefficient is  $\mu_f = 0.7$ , low-temperature plasticity is defined exactly as derived by the  
 269 laboratory study of Mei et al. (2010), high-temperature creep is formulated following Zhong &  
 270 Watts (2013), and we set the activation temperature  $T_{HTC} = 800$  °C (Tables 1 and 2). The  
 271 evolution of surface flexure, internal viscosity, stress and strain fields are shown at  $t=0$  (Figure  
 272 4a-d),  $t=12.5\tau_M$  (Figure 4e-h), and  $t=500\tau_M$  (Figure 4i-l). At  $t=500\tau_M$ , surface flexure is maximal  
 273 (Figure 4i), the lithosphere is thinned beneath the load due to nonlinear weakening (Figure 4j),  
 274 the load is supported by lithospheric stress (Figure 4k), and the strain rate is negligible indicating  
 275 a steady state (Figure 4l). The steady state surface flexure is best-reproduced by a two-layer  
 276 model with  $T_e = 64$  km which indicates that  $T_e$  of the complex viscoelastic lithosphere in Case 1h  
 277 is 64 km (Figure 4m-p). We note that  $T_e = 64$  km would be unusually high for 90 Ma oceanic  
 278 lithosphere.

279 In Suite 1, we compute the evolution of a suite of models that are identical to Case 1h except  
 280 the age of the lithosphere is varied in 10 Ma increments from 20 Ma to 130 Ma. The predictions  
 281 of  $T_e$  from Suite 1 approximately follow the 800 °C isotherm, which increases from  $\sim 25$  km  
 282 depth at 20 Ma, to  $\sim 80$  km depth at 130 Ma (Figure 5b, Table 2). Note that we have set the  
 283 threshold temperature  $T_{HTC} = 800$  °C.

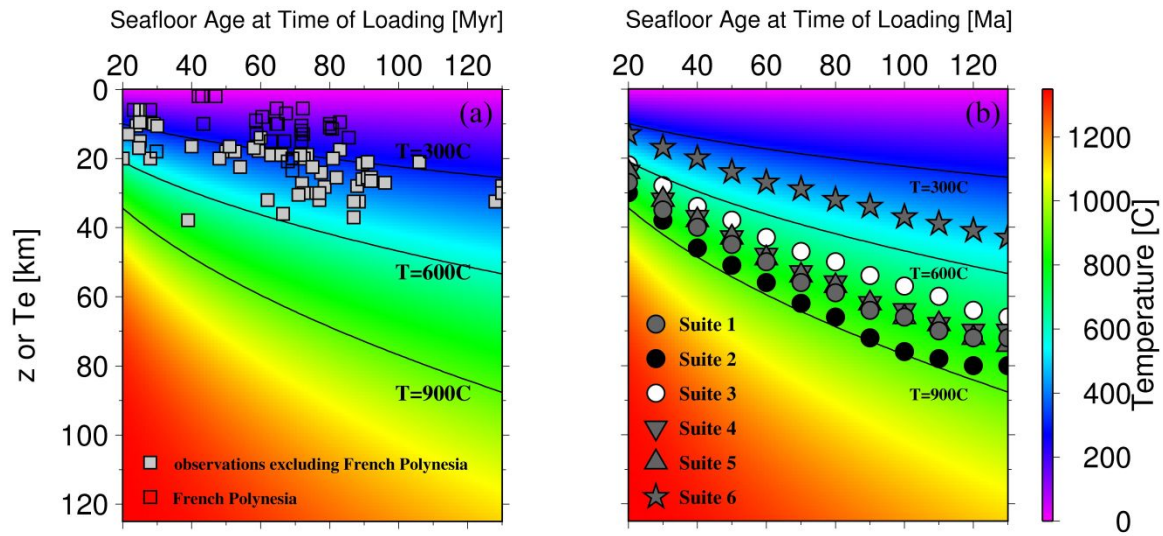


**Figure 5. Observed and predicted elastic thickness,  $T_e$ .** Observed (a) and predicted (b) elastic thickness as a function of seafloor age supposed on a colormap which shows the thermal structure based on the half-space cooling model. Black lines show isotherms for 300 °C, 600 °C, and 900 °C. In Suite 1,  $\mu_f=0.7$ ,  $E_{LTP}=320$  kJ/mol,  $A_0=3$  km, and  $T_{HTC}=800$  °C where  $\mu_f$  is the frictional coefficient,  $E_{LTP}$  is the activation energy of low-temperature plasticity,  $A_0$  is the trapezoidal load amplitude, and  $T_{HTC}$  is the activation temperature for high-temperature creep. All other suites are identical to Suite 1 except for the following modifications. In Suite 2,  $T_{HTC}$  is increased to 900 °C. In Suite 3,  $T_{HTC}$  is decreased to 600 °C. In Suite 4,  $A_0$  is increased to 6 km. In Suite 5,  $\mu_f$  is decreased to 0.3. In Suite 6,  $E_{LTP}$  is decreased to 190 kJ/mol.

We increase  $T_{HTC}=900$  °C in Suite 2 and leave all other parameters unchanged relative to Suite 1. In Suite 2, the  $T_e$  approximately follows the 900 °C isotherm (Figure 5b, Table 2). The reason for which  $T_e$  approximately follows the isotherm of  $T_{HTC}$  in Suites 1 and 2 is made clear by Figure 2a, where laboratory-derived rheology predicts a large yield stress (i.e., high viscosity) for low-temperature plasticity, which drastically reduces upon the transition to high-temperature creep (i.e., when temperature exceeds  $T_{HTC}$ ). However, reducing  $T_{HTC}$  indefinitely should not necessarily reduce  $T_e$  to arbitrarily small values, because the strength of high-temperature creep also becomes quite large at intermediate depths and temperatures (e.g., 400-600 °C). For example, when  $T_{HTC}$  is equal to 600 °C in Suite 3, and the effective  $T_e$  approximately follows the 700 °C isotherm. This indicates that reducing  $T_{HTC}$  to even smaller values will not reduce the predicted  $T_e$  any further, because high-temperature creep is no weaker than low-temperature plasticity at temperatures less than ~700 °C. Therefore, this estimate represents a lower-bound for  $T_e$  based on laboratory-derived rheology and a load with amplitude  $A_0=3$  km and density  $\rho=3330$  kg/m<sup>3</sup>.

In Suite 4, we test the effects of a larger load with amplitude  $A_0=6$  km which corresponds to a normal stress consistent with the largest seamounts and ocean islands on Earth (e.g., Hawaii, Tenerife). All other aspects of the models are identical to those of Suite 1. Relative to Suite 1, the predictions of  $T_e$  from Suite 4 are smaller by 1-4 km or 1-15%, and still fall between the 600-900 °C isotherms or ~25-80 km depth (Figure 5b, Table 2). This demonstrates that the stress-dependence of lithospheric rheology cannot significantly reduce estimates of  $T_e$  based on reasonable variations in load size.

In Suite 5, we test the sensitivity of  $T_e$  to the frictional coefficient of faults by reducing the frictional coefficient from  $\mu_f=0.7$  to  $\mu_f=0.3$  (Bellas & Zhong, 2021) and all other aspects are

consistent with Suite 1 ( $A_0=3$  km,  $T_{HTC}=800$  °C). In Suite 5,  $T_e$  falls along the 800 °C isotherm for increasing seafloor age similar to Suites 1-4 which demonstrates a weak influence of the  $\mu_f$  on  $T_e$  consistent with previous studies (Figure 5b, Table 2) (Zhong & Watts, 2013). We have also tested the flexural response against the influence of non-zero cohesion equal to 75 MPa, and the influence of formulating frictional sliding to be sensitive to the differing strength of normal and reverse faults and found very weak sensitivity in both cases. It is worth noting that Zhong & Watts (2013) also found a weak influence of high-temperature creep on flexure provided the reference viscosity of the mantle is reasonable (e.g.,  $<10^{22}$  Pa s) and for this reason, we do not test the effects of varying high-temperature creep in this study.

In Suite 6, low-temperature plasticity is modified such that the activation energy,  $E_p$ , is reduced from 320 kJ/mol (Mei et al., 2010) to 190 kJ/mol (Figure 2c) because previous studies have shown that flexure at Hawaii may be reproduced by laboratory-derived flow laws including that of Mei et al. (2010) if the activation energy for low-temperature plasticity,  $E_p$ , is reduced as such (e.g., Bellas et al., 2020). All other aspects of Suite 6 are identical to those of Suite 1. In Suite 6,  $T_e$  is reduced by a factor of approximately two compared to Suites 1-5 and falls along the  $\sim 450$  °C isotherm depth, or  $\sim 10$ -40 km depth for seafloor age 20-130 Ma (Figure 5b, Table 2). The significance of this result is that the only appreciable perturbation to  $T_e$  comes from a significant reduction in the strength (viscosity or yield stress) of low-temperature plasticity, consistent with previous studies (Zhong & Watts, 2013; Bellas et al., 2020). Meanwhile, reasonable variations in the load amplitude  $A_0$  (Suite 4), in the creep activation temperature  $T_{HTC}$  (Suites 1-3), or in the frictional coefficient  $\mu_f$  (Suite 5), produce only minor variations in  $T_e$ .

We now introduce the global dataset of observationally-inferred  $T_e$  estimates, with which results from Suites 1-6 will be compared (Figure 5a). Note that isolated seamounts and islands



(e.g., Bermuda) may form by a different mechanism than those associated with hotspot tracks (e.g., Hawaii, Louisville). The observational catalogue includes 101 estimates of  $T_e$  based on flexural systems which span the global oceans, 31 of which are derived from French Polynesia (for details, refer to Watts & Zhong, 2000). The vast majority of observationally inferred  $T_e$  estimates lie between the 300-600 °C isotherms, although estimates from French Polynesia are anomalous (Figure 5a; Watts, 2001; Watts & Zhong, 2000). It is generally thought that the anomalously low  $T_e$  estimates derived from French Polynesia represent oceanic lithosphere that has been significantly modified by interaction with the South Pacific Isotopic and Thermal Anomaly (SOPITA) (Smith et al., 1989). There is also appreciable spread in the  $T_e$  dataset for standard settings (i.e., between the 300-600 °C isotherms) which may be related to the varying degrees of plume and magmatic activity at different ocean island systems, or to the methods that were used to infer  $T_e$  which span a large body of work published since 1970 (Watts & Zhong, 2000). However, the general consensus is that  $T_e$  estimates excluding French Polynesia are standard, while  $T_e$  at French Polynesia is anomalous.

In comparison, for Suites 1-5, all of which include laboratory-derived low-temperature plasticity, the predictions exceed the standard observations of  $T_e$  by a factor of approximately two, and observations from French Polynesia by even more. Meanwhile, the standard observations are accurately reproduced by Suite 6 which includes modified low-temperature plasticity. Therefore, we have demonstrated for the first time that laboratory-derived lithospheric rheology significantly overestimates  $T_e$  at most oceanic-plate interior settings, not just the Hawaiian Islands. In conclusion, we have shown that Hawaiian lithosphere is not anomalous in terms of elastic thickness (i.e., rheology, thermal structure, magmatic effects), and the

352 conundrum that the yield stress of oceanic lithosphere appears stronger at subduction zones than  
 353 ocean islands remains unsolved.

**Table 2. Infinite Plate Models**

Case	thermal age [Ma]	$A_0$ [km]	$T_{HTC}$ [°C]	$E_{LTP}$ [kJ/mol]	$\mu_f$	$w_0$ [m]	$T_e^{FE}$ [km]	$T_e^{YSE}$ [km]
1a	20	3	800	320	0.7	1337	27	28
1b	30	3	800	320	0.7	1129	35	35
1c	40	3	800	320	0.7	1017	40	43
1d	50	3	800	320	0.7	933	45	48
1e	60	3	800	320	0.7	866	50	52
1f	70	3	800	320	0.7	802	56	56
1g	80	3	800	320	0.7	777	59	60
1h	90	3	800	320	0.7	733	64	63
1i	100	3	800	320	0.7	709	66	68
1j	110	3	800	320	0.7	687	70	72
1k	120	3	800	320	0.7	666	72	75
1l	130	3	800	320	0.7	647	76	78
2a	20	3	900	320	0.7	1241	30	30
2b	30	3	900	320	0.7	1057	38	42
2c	40	3	900	320	0.7	933	46	49
2d	50	3	900	320	0.7	859	51	53
2e	60	3	900	320	0.7	800	56	60
2f	70	3	900	320	0.7	750	62	65
2g	80	3	900	320	0.7	709	66	69
2h	90	3	900	320	0.7	672	72	74
2i	100	3	900	320	0.7	650	76	77
2j	110	3	900	320	0.7	630	78	81
2k	120	3	900	320	0.7	603	84	86
2l	130	3	900	320	0.7	587	86	90
3a	20	3	600	320	0.7	1551	22	18
3b	30	3	600	320	0.7	1312	28	29
3c	40	3	600	320	0.7	1162	34	32
3d	50	3	600	320	0.7	1059	38	36
3e	60	3	600	320	0.7	984	43	43
3f	70	3	600	320	0.7	923	47	45
3g	80	3	600	320	0.7	873	50	50
3h	90	3	600	320	0.7	832	54	54
3i	100	3	600	320	0.7	796	57	57
3j	110	3	600	320	0.7	765	60	60
3k	120	3	600	320	0.7	738	64	63
3l	130	3	600	320	0.7	714	66	67
4a	20	6	800	320	0.7	2892	24	26
4b	30	6	800	320	0.7	2405	32	31
4c	40	6	800	320	0.7	2143	37	38

4d	50	6	800	320	0.7	1953	43	44
4e	60	6	800	320	0.7	1806	48	51
4f	70	6	800	320	0.7	1681	53	54
4g	80	6	800	320	0.7	1607	56	59
4h	90	6	800	320	0.7	1515	62	63
4i	100	6	800	320	0.7	1462	64	66
4j	110	6	800	320	0.7	1414	68	70
4k	120	6	800	320	0.7	1367	70	74
4l	130	6	800	320	0.7	1327	74	75
5a	20	3	800	320	0.3	1430	24	24
5b	30	3	800	320	0.3	1184	32	35
5c	40	3	800	320	0.3	1056	38	39
5d	50	3	800	320	0.3	962	43	45
5e	60	3	800	320	0.3	889	49	51
5f	70	3	800	320	0.3	826	54	54
5g	80	3	800	320	0.3	792	57	59
5h	90	3	800	320	0.3	745	62	62
5i	100	3	800	320	0.3	720	66	67
5j	110	3	800	320	0.3	697	68	70
5k	120	3	800	320	0.3	675	72	74
5l	130	3	800	320	0.3	655	74	78
6a	20	3	800	190	0.7	2124	13	14
6b	30	3	800	190	0.7	1829	17	16
6c	40	3	800	190	0.7	1639	20	20
6d	50	3	800	190	0.7	1491	24	25
6e	60	3	800	190	0.7	1366	27	29
6f	70	3	800	190	0.7	1255	29	32
6g	80	3	800	190	0.7	1218	32	34
6h	90	3	800	190	0.7	1153	34	35
6i	100	3	800	190	0.7	1099	37	40
6j	110	3	800	190	0.7	1053	39	42
6k	120	3	800	190	0.7	1022	41	44
6l	130	3	800	190	0.7	987	43	45

\* $A_0$  is the load amplitude,  $T_{HTC}$  is the activation temperature for high-temperature creep,  $E_{LTP}$  is the plastic activation energy,  $\mu_f$  is the frictional coefficient,  $w_0$  is the maximum surface flexure,  $T_e^{FE}$  is the elastic thickness based on numerical models, and  $T_e^{YSE}$  is the elastic thickness based on the YSE method. Cases are organized into suites, within which only the thermal age is varied except for a few select cases marked with the symbols.

### 3.2 The Yield Stress Envelope Method and Fully Dynamic Models of Flexure

In this section, we test whether the YSE method reproduces  $T_e$  of fully dynamic viscoelastic loading models and examine the sensitivity of the YSE method to error in the curvature and strain rate which are required as inputs but not necessarily well-constrained in observational studies. The overarching goal is to determine whether the YSE method, which was used to constrain lithospheric rheology at subduction zones (Hunter & Watts, 2016), is associated with systematic error that may explain the discrepancy between the rheology of subducting lithosphere (equivalently, that derived in laboratory experiments), and that of oceanic plate interiors.

In the following, we present results from the 2D numerical model, Case 1h, that are relevant to the YSE method. Recall that Case 1h was previously present in section 3.1 and has 90 Ma lithospheric thermal structure and load amplitude  $A_0=3$  km (Figures 2, 4, 5, and Table 2). At  $t=500\tau_M$  Case 1h is in steady state, the maximum surface flexure is  $\sim 700$  m, and the two-layer model which best-reproduces flexure has  $T_e=64$  km (Figure 6a). In addition, the maximum curvature is  $\sim 10^{-8} \text{ m}^{-1}$  which occurs in the trench outer-slope region (Figure 6a) where observations from real flexure systems are most often available (Craig et al., 2014). The 1D vertical stress profile is taken at the location of maximum curvature and shows that elastic bending stresses reach  $\sim 50$  MPa and are truncated by frictional sliding near the surface, and by high-temperature creep below  $\sim 65$  km depth (Figure 6b). Low-temperature plasticity is not activated in the 1D vertical stress profile because bending stresses are not large enough to intersect the yield stress of low-temperature plasticity (compare Figure 6b with Figure 2a). In other words, deformation is purely elastic except for yielding by frictional sliding and high-

376 temperature creep near the surface and at depth, respectively, because low-temperature plasticity  
 377 is so strong in Case 1h.

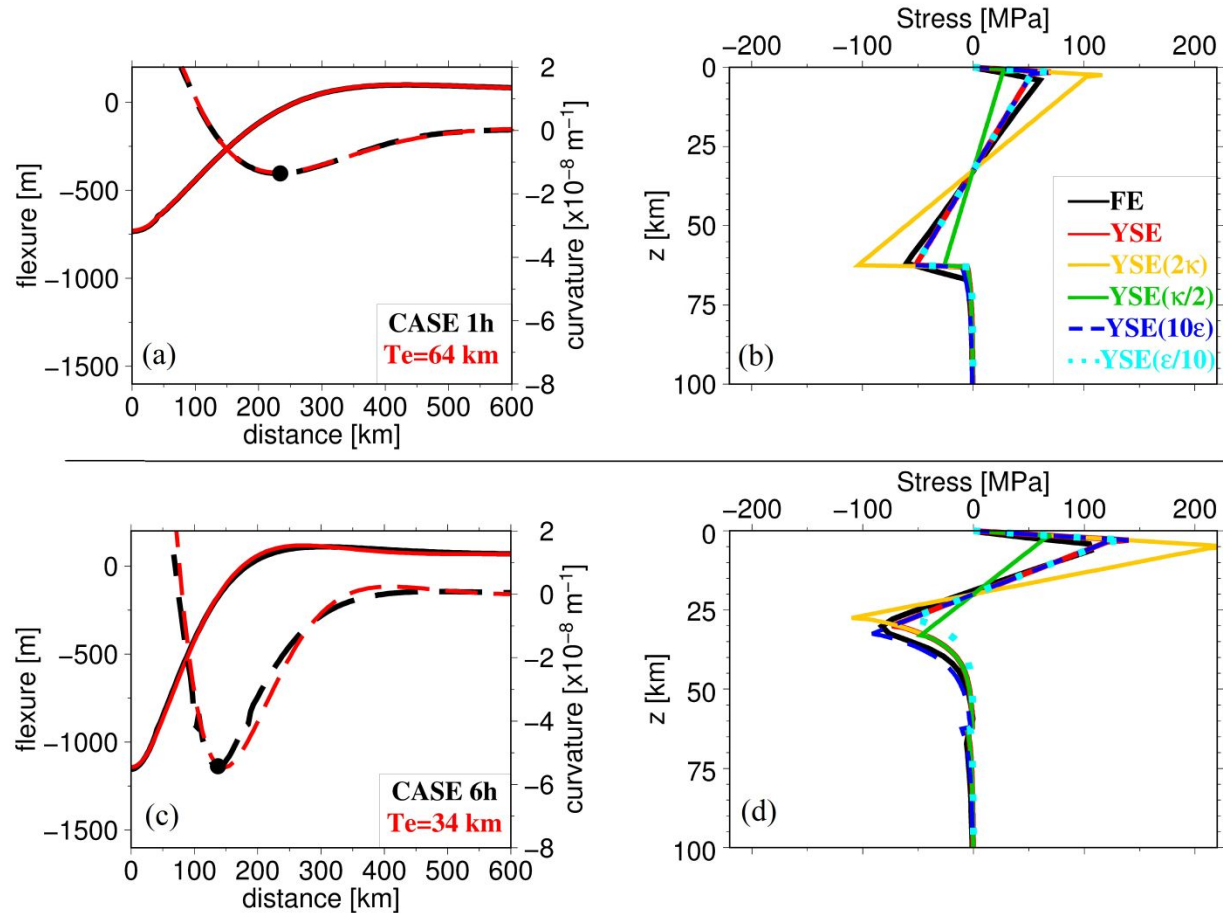


**Figure 6. The yield stress envelope method and fully dynamic viscoelastic loading models.** (a) The flexure (solid) and surface curvature (dashed) from Case 1h and the best-fit two-layer model, which has  $T_e=64$  km. Only half of the flexural profile is shown, which is reflected across  $x=0$  km. The black dot marks the maximum curvature. (b) The differential stress profile taken from Case 1h at the location of maximum curvature (FE for finite element), and the stress profiles predicted by the YSE method for accurate inputs (red, YSE), for curvature that is too large by a factor of two (yellow, YSE( $2\kappa$ )), for curvature that is too small by a factor of two (green, YSE( $\kappa/2$ )), for strain rate that is too large by a factor of 10 (blue, YSE( $10\dot{\epsilon}$ )), and for strain rate that is too small by a factor of 10 (cyan, YSE( $\dot{\epsilon}/10$ )). (c) Same as (a), but for Case 6h. (d) Same as (b) but for Case 6h.

We use results from the numerical Case 1h to construct the corresponding YSE, and to determine  $T_e$  based on the YSE method in following steps. First, the YSE is constructed by predicting the yield stress of frictional sliding, which is a simple function of depth (equation 1). Second, the average strain rate in the lithosphere while the surface is actively deflecting ( $\dot{\epsilon}=10^{-16}$  s<sup>-1</sup>, Figure 4h) and a 90 Ma thermal structure are used to solve the yield stresses of low-temperature plasticity and high-temperature creep (equation 2 and equation 3, respectively). Third, the maximum curvature in the flexural bulge region from Case 1h is used to predict the elastic bending stress (equation 5). Fourth, the bending moment is given by the vertical integral of the YSE and elastic bending stresses (Figure 6b; equation 4). Finally, this bending moment is equated to the expression for the bending moment of a purely elastic plate (equation 6) such that  $T_e$  can be solved. Note that the depth of the neutral plane,  $z_n$ , is constrained by the requirement that the integral of stresses above and below it cancel out.

When the YSE method is applied in this manner with inputs taken directly from Case 1h, the elastic thickness estimate is  $T_e=64$  km, which reproduces the true or numerical value of 64 km exactly (Table 2), thus validating the YSE method. This is what we expect given that the YSE constructed in this manner produces good agreement with the 1D vertical stress profile taken directly from the numerical model, Case 1h (Figure 6b).

We also test the sensitivity of the YSE method to error in strain rate and curvature since these parameters may be associated with significant uncertainty in observational studies. Curvature controls the slope of elastic bending stress with depth (equation 5), while strain rate controls the yield stresses of the ductile deformation mechanisms (e.g., equation 2 and equation 3). First, if the curvature used as input to the YSE is increased by a factor of two, then the slope of elastic

bending stresses increases by a factor of two, and larger bending stresses activate yielding by frictional sliding and high-temperature creep to greater degree (Figure 6b). If the YSE method is applied as outlined above, but uses curvature that is too large by a factor of two, then the predicted  $T_e$  is reduced from 64 km to 63 km. This is because increasing the curvature is equivalent to increasing the degree of nonlinear weakening. Similarly, if curvature is reduced by a factor of two, then the YSE method estimate of  $T_e$  increases to 70 km (Figure 6b). This demonstrates that the YSE method applied to Case 1h is not very sensitive to error in the assumed curvature. Second, we test the sensitivity to error in the assumed strain rate. We test decreasing the strain rate from  $10^{-16} \text{ s}^{-1}$  to  $10^{-17} \text{ s}^{-1}$  and the effect is to decrease the yield stress of the ductile deformation mechanisms (equation 2 and equation 3; Figure 6b), such that the YSE method predicts  $T_e=63$  km. Similarly, if the strain rate is increased to  $10^{-15} \text{ s}^{-1}$ , the effect is to increase the yield stress of low-temperature plasticity and high-temperature creep (Figure 6b), and the YSE method predicts  $T_e=66$  km. In summary, our results show that the YSE method is modestly sensitive to error in both strain rate and curvature in Case 1h, where error in  $T_e$  is always less than 10%.

Having analyzed the YSE method applied to Case 1h in some detail, we now apply the YSE method similarly to all cases in Suite 1, as well as to Suites 2-6 (Table 2). To be clear, the maximum curvature and average strain rate in the lithosphere are taken from each numerical model and used as input for each corresponding YSE and the prediction of  $T_e$ . The results are summarized in Table 2, and the main result is that the YSE method reproduces the  $T_e$  of the numerical models within  $\sim 10\%$  errors, despite limitations such as being unable to account for spatial and temporal variations in strain rate and curvature.

Detailed results and sensitivity tests are also presented for Case 6h, for which the lithosphere is much weaker, the degree of bending is greater, and the predicted  $T_e$  is consistent with observationally inferred values for 90 Ma oceanic lithosphere (Figure 5a, 6c-d). The YSE method applied to Case 6h predicts  $T_e=37$  km compared to the fully dynamic value  $T_e=34$  km. In addition, curvature that is too large or too small by a factor of two causes the YSE method to predict  $T_e$  is 32 km and 41 km, respectively, while strain rate that is too large ( $10^{-15} \text{ s}^{-1}$ ) or too small ( $10^{-17} \text{ s}^{-1}$ ) causes the YSE method to predict  $T_e$  is 41 km or 33 km, respectively.

These results indicate that the YSE method is more sensitive to error when applied to systems with a greater degree of bending, with up to 21% error associated with overestimation of  $T_e$ , but up to only 6% error for underestimation. Whether the YSE method overestimates or underestimates  $T_e$  is important because significant underestimation of  $T_e$  could lead to the association of reasonable  $T_e$  values with laboratory-derived rheology, even though our previous results suggest it is too strong (e.g., Figure 5). However, our results show that the YSE method is not very susceptible to underestimating  $T_e$  when subject to error in the strain rate and curvature used as input.

In summary, we have tested a wide variety of loading scenarios on infinite plates which are representative of most oceanic plate interior flexure systems (Table 2). The results show that the YSE method performs well for a wide range of  $T_e$  (15-89 km), rheological parameter values (Tables 1-2), thermal structures (20-130 Ma), and trapezoidal load amplitudes (3-6 km) for load density  $\rho=3330 \text{ kg/m}^3$ . Furthermore, the YSE method is not particularly sensitive to error in either the curvature or the strain rate when applied to a system with modest flexure (<10% error is maintained), although this sensitivity increases as the degree of flexure increases. When applied to systems subject to a significant degree of flexure (e.g., curvature  $\sim 10^{-7} \text{ m}^{-1}$ ), the YSE



method may overestimate  $T_e$  by up to 20%, but underestimates  $T_e$  by no more than 6%. Therefore, it seems unlikely that error from the YSE method can explain why laboratory-derived rheology, which is too strong compared to plate interior settings, appears consistent with subducting lithosphere in recent studies (Hunter & Watts, 2016).

### 3.3 Testing the Broken Elastic Plate Model Against Fully Dynamic Models of Flexure

The broken elastic plate model (BEPM) has been widely used to model lithospheric flexure at subduction zones (e.g., Bodine et al., 1981; Hunter & Watts, 2016), foreland basins (Lyon-Caen & Molnar, 1983), oceanic fracture zones (Wessel & Haxby, 1990), and even oceanic islands (e.g., Watts & ten Brink, 1989; Wessel, 1993) with much success in reproducing the morphology of bending at such settings (i.e., bending with uniformly concave-downward curvature). The BEPM has recently been used in tandem with the YSE method to constrain the rheology of subducting lithosphere at circum-Pacific subduction zones (Hunter & Watts, 2016). Since we demonstrated that the YSE method accurately reproduces  $T_e$  in the previous section 3.2, we now investigate the BEPM to test whether it is accurate and appropriate for modeling flexure at subduction zones.

In the following, we modify the viscoelastic loading model to have a reduced viscosity zone near  $x=0$  km which effectively imposes a free edge and mimics the geometry of the BEPM (e.g., Figure 3d). The viscoelastic loading models are distinct from the BEPM in that they are subject to a finite-width load and the bending moment is not independently varied, but we suggest that the effects of a line load on the free edge of an elastic plate model are similar. As in previous sections, we estimate  $T_e$  based on the minimum misfit two-layer model (note that the two-layer models do not include a free edge).

Case 7a with a continuous (i.e., unbroken) plate will serve as a reference model. Case 7a is identical to Case 1h except that the trapezoidal load amplitude is increased to 10 km to reflect

larger loads in subduction zones (Table 3). The steady state solution of flexure and the viscosity field are presented in Figure 7a, where the flexure is  $\sim 2500$  m and the viscosity field shows evidence of nonlinear weakening beneath the surface load (i.e., near  $x=0$ ). The two-layer model which reproduces the flexure of Case 7a with minimum misfit has  $T_e=58$  km.

Case 7b is identical to Case 7a except viscosity is reduced to  $10^{21}$  Pa s in the lithosphere between  $x=0$  km and  $x=8$  km where 4 elements resolve the weak zone (Figure 3d; Figure 7b). This weak zone is imposed to simulate a free edge, the geometry of the BEPM, and real Earth systems in which a free edge arises because of the existence of an adjacent weak zone. This model configuration is also similar to that of a 1D cantilever beam that is fixed at one end. As a result of imposing this weak zone, the maximum flexure of the competent lithosphere occurs at the free edge ( $\sim 3000$  m, Figure 7b), and the curvature is now uniformly concave down. The flexure of the weak zone is much greater than the competent lithosphere but will be ignored in our analysis because its only purpose is to simulate a free edge. The flexure of the competent lithosphere ( $x>20$  km) is best-reproduced by a two-layer model with  $T_e=36$  km. Note that this  $T_e=36$  km is  $\sim 38\%$  smaller than that of Case 7a (Table 3).

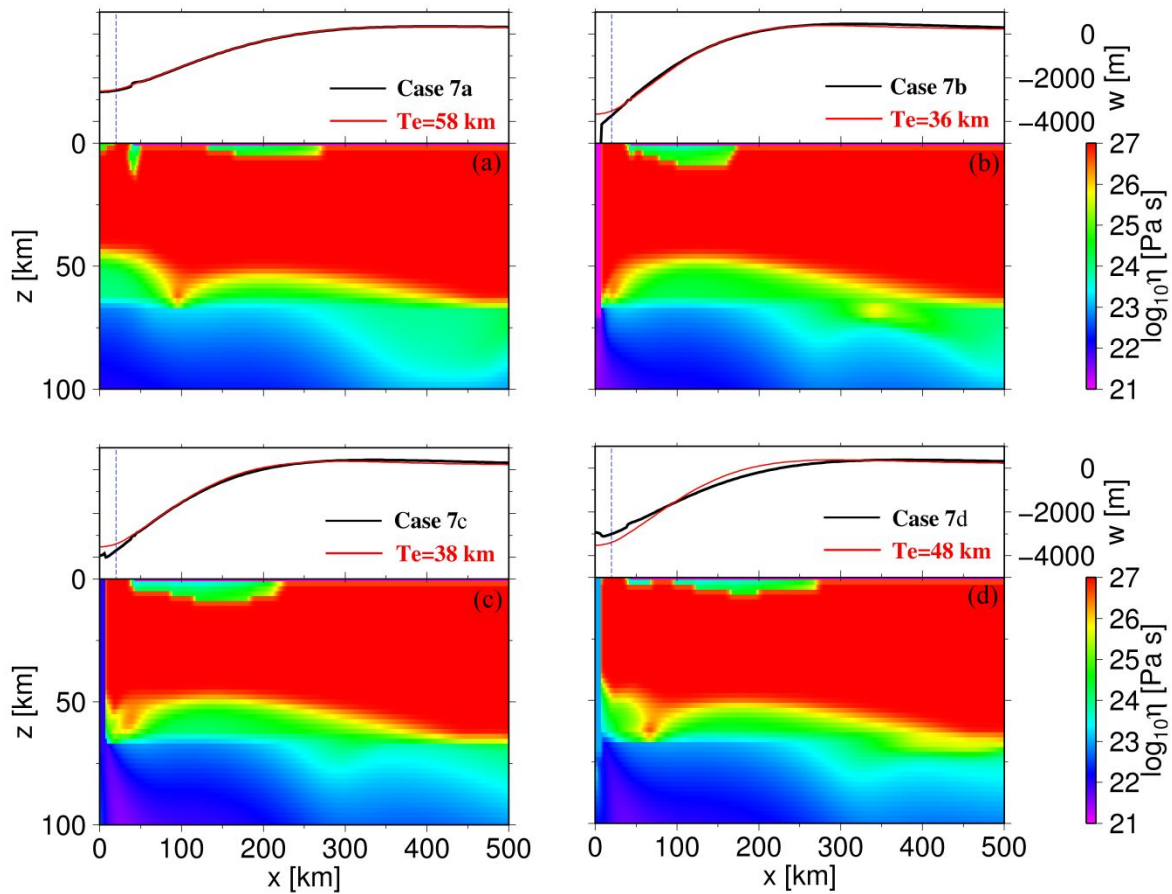


**Figure 7. The effect of introducing a free edge in models of flexure.** All results are symmetric across  $x=0$ . (a) The steady state flexure and viscosity field for Case 7a with infinite or continuous lithosphere (black), and the best-fit two-layer model (red). The vertical dashed blue line shows the leftmost extent to which the misfit to flexure is calculated. (b) Similar results are presented for Case 7b which has a weak zone with viscosity  $10^{21}$  Pa s imposed in the lithosphere between  $x=0$  km and  $x=8$  km, (c) for Case 7c in which the weak zone viscosity is  $10^{22}$  Pa s, and (d) Case 7d in which the weak zone viscosity is  $10^{23}$  Pa s. This model configuration mimics the semi-infinite geometry and free edge of the BEPM.

In the following, we investigate the sensitivity of the results to the properties of the weak zone. In Case 7c the viscosity of the weak zone is increased to  $10^{22}$  Pa s (Figure 7c), and all other aspects of the model are identical to Case 7b. The elastic thickness  $T_e=38$  km and slightly larger than in Case 7b (36 km), which reflects the increased strength associated with the higher viscosity assigned to the weak zone (Table 3). Next, the viscosity of the weak zone is increased to  $10^{23}$  Pa s in Case 7d, and results are presented in Figure 7d. The effective elastic thickness  $T_e=48$  km and significantly larger than Cases 7b and 7c (Table 3). This indicates that the flexural response of the system approaches that of the continuous plate as the viscosity of the weak zone is increased, as expected.

We also investigate sensitivity of the results to the weak zone width. In Case 7e, the weak zone width is increased from 8 km to 12.5 km, but we do not present results visually because they are not significantly different from those of Case 7d (Figure 7d). In Case 7e, the effective elastic thickness  $T_e=46$  km, indicating that a wider weak zone imparts more weakening to the system. Finally, in Case 7f, the weak zone width is increased to 19 km, and the effective elastic thickness  $T_e=44$  km, which also supports the idea that a larger weak zone imparts more weakening.

**Table 3. Broken Plate Models**

case	$E_{LTP}$ [kJ/mol]	$T_e^{FE}$ [km]	$\eta_{WZ}$ [Pa s]	$\Delta x_{WZ}$ [km]
7a*	320	58	N/A	N/A
7b	320	36	$10^{21}$	8
7c	320	38	$10^{22}$	8
7d	320	48	$10^{23}$	8
7e	320	46	$10^{23}$	12.5
7f	320	44	$10^{23}$	19

\*In all cases, the thermal age of the lithosphere is 90 Ma, the trapezoidal load amplitude  $A_\theta=10$  km, the high-temperature creep activation temperature  $T_{HTC}=800$  °C, and the frictional coefficient  $\mu_f=0.7$ . The viscosity of the weak zone is  $\eta_{WZ}$ , and the width of the weak zone is  $\Delta x_{WZ}$ . Case 7a is a reference model with unbroken lithosphere.

The significance of these results is that the flexural response to a load is highly sensitive to the existence of a free edge and the degree to which it is viscously coupled to the adjacent weak zone. Cases 7b-g with free edges and adjacent weak zones demonstrate a significant reduction in the net flexural strength of the whole system relative to the continuous lithosphere of Case 7a (up to 38%). This indicates that the net flexural strength of the system is not only a function of the plate thickness, but also of the properties of the adjacent weak zone (i.e., free edge). Therefore, applying the BEPM to a real Earth system could significantly bias the inferred plate thickness (i.e., strength and rheology). In particular, if the free edge in the model is a source of weakness relative to the real Earth system, then tradeoff with the inferred plate thickness may occur to conserve the net flexural strength, where the net flexural strength is constrained by observations of flexure and loads. This could lead to overestimation of the plate strength and would have

important implications for previous constraints on rheology that were based on the BEPM (e.g., Hunter & Watts, 2016).

#### **4. Discussion**

The distribution of stress and strain in a bending plate is of great interest because it elucidates the physical properties of the lithosphere. However, only simplified formulations of the physics of bending have been available to investigate flexural systems until quite recently. For example, the solutions of the classic elastic plate model (EPM), broken elastic plate model (BEPM), and the yield stress envelope (YSE) method, all rely on the thin plate approximation and other assumptions. Furthermore, deformation mechanisms including frictional sliding, low-temperature plasticity, and high-temperature creep have been observed and quantified in mineral physics experiments, but laboratory conditions are considerably different from those in the lithosphere (e.g., strain rate). While some recent studies (Hunter & Watts, 2016) indicated that laboratory-derived rheology is consistent with the flexure of subducting lithosphere based on the BEPM and the YSE method, other studies have demonstrated that laboratory-derived rheology is too strong relative to field observations at the Hawaiian Islands (Zhong & Watts, 2013; Bellas et al., 2020). This study seeks to understand the source of the apparent discrepancy in the yield stress of oceanic lithosphere, where oceanic lithosphere appears stronger at plate boundaries than at plate interiors, by investigating the methods that have been used to infer elastic thickness.

##### **4.1 The Yield Stress Envelope Method and the Broken Elastic Plate Model**

We show that the YSE method accurately reproduces the effective elastic thickness,  $T_e$ , to within 10% error of viscoelastic loading models for a broad range of rheological parameters, thermal structures, and load amplitudes (Table 2, Figure 6). We also show that the YSE method is not very sensitive to error in the strain rate and curvature when applied to a system with

modest flexure (e.g., curvature  $\sim 10^{-8} \text{ m}^{-1}$ ). Even for a factor of ten error in curvature and strain rate,  $T_e$  as estimated by the YSE method is never underestimated by more than 6%. Therefore, it is not likely that the YSE method caused rheology that is actually too strong to appear consistent with observations at subduction zones by underestimating  $T_e$  in previous studies, and our investigation of the YSE method did not resolve the conundrum of strong oceanic plate boundaries relative to plate interiors.

In our investigation of the BEPM, we showed that introducing a free edge in models of flexure significantly enhances the flexural response to a load and reduces the effective  $T_e$  of the system as a whole. In addition, the degree to which the flexural response is enhanced is highly sensitive to the properties of the weak zone. The significance of this result is that the BEPM assumes a completely unconstrained free edge, but is applied to model real Earth systems that are not necessarily free to equal degree. For example, at subduction zones, the subducting plate is generally continuous, and likely maintains some finite strength and mechanical coupling to the down-going portion of the slab as it traverses the trench and beyond. However, this finite strength is completely neglected in the BEPM which may, therefore, contain a source of weakness at the free edge relative to the real Earth system. To be clear, we are not suggesting that the continuous or infinite EPM is a better option for modeling flexure at subduction zones. Rather, we are pointing out a potentially critical difference between the BEPM and the real Earth systems to which it is applied.

If the free edge in the BEPM is weaker than the corresponding location in the real Earth system, then the BEPM will infer a higher  $T_e$  to compensate for the relative weakness of the free edge. For example, previous studies have shown that the BEPM infers a significantly larger  $T_e$  than the EPM when applied to fit observations of flexure at Hawaii (Watts & ten Brink, 1989;

Wessel, 1993). Therefore, we suggest that exactly this type of tradeoff may arise between the free edge and the inferred plate thickness in the BEPM, and if this is the case, then results from recent studies which used the BEPM to constrain lithospheric rheology at subduction zones may be called into question.

## 4.2 Rheology of the Lithosphere at Ocean Island Settings

We have shown that laboratory-derived rheology overestimates  $T_e$  by a factor of two at standard ocean island settings, and by a factor greater than two at French Polynesia where  $T_e$  is anomalously low (Figure 5). We consider it highly unlikely that plume- and magmatic-activity would modify the lithosphere to equal degree at many seamounts and ocean islands, especially those with much weaker plume-activity and volcanism than that at the Hawaiian Islands (e.g., the Canary Islands, the Island of Mayotte, or Bermuda). Therefore, our new results support the conclusion of Zhong & Watts (2013) and Bellas et al. (2020) that laboratory-derived low-temperature plasticity significantly overestimates the yield stress of the Hawaiian lithosphere, and show that this conclusion also applies to oceanic lithosphere at ocean island settings in general.

Other studies (e.g., Pleus et al., 2020; Buck et al., 2015) have suggested that a modification to laboratory-derived rheology is not necessary, and rather that the Hawaiian lithosphere is anomalously warm and/or magmatically fractured. We acknowledge that regional thermal rejuvenation by a plume could bring laboratory-derived rheology or Suites 1-5 into agreement with observations, but that the required amount of warming corresponds to a reduction in thermal age from 60 Myr to 20 Myr, from 100 Myr to 30 Myr, or ~67% reduction (Figure 5) which is not supported by observations of heat flux at the Hawaiian Islands (von Herzen et al., 1989) nor Cape Verde (Courtney & White, 1986), swell topography at 14 ocean island settings (Huppert et



al., 2020), nor admittance ratios at the Hawaiian Islands (Cadio et al., 2012). We also acknowledge that laboratory-derived rheology could reproduce observed  $T_e$  if magmatic diking and intrusion impart a reduction in lithospheric viscosity to mantle viscosity ( $10^{21}$  Pa s) over a region that penetrates coherently through all depths in the lithosphere and over a finite width of a few km and is effectively infinite in length (Cases 7a and 7b), but this is not supported by seismic observations of small isolated magma chambers and conduits (Laske et al., 2011; Wright & Klein, 2006) nor the continuous distribution of seismicity across lithospheric depths (Klein, 2016) at the Hawaiian Islands where volcanism is generally considered to be of greatest intensity on Earth.

It is also important to consider the possibility that oceanic lithosphere is always anomalous at ocean island settings at the time of loading relative to a standard oceanic lithosphere due to thermomechanical erosion by plumes and the weakening effects of magmatic plumbing systems. However, we consider it highly unlikely that such anomalies have led to a consistent factor of two reduction in  $T_e$  at most ocean island settings given the varying degrees of plume- and volcanic-activity. For example, we would expect for the greatest amount of thermal and magmatic weakening to be associated with the Hawaiian Islands, but  $T_e$  at the Hawaiian Islands is 30-35 km and slightly larger than most other estimates of  $T_e$  for 90 Ma seafloor at the time of loading (Figure 5a).

Previous studies have demonstrated that the flexural strength of the lithosphere is primarily controlled by low-temperature plasticity (Zhong & Watts, 2013), and we reinforce here that the only way to bring laboratory-based predictions into agreement with observations of  $T_e$  is to reduce its strength (i.e., yield stress or effective viscosity). We show that reducing the activation

energy of the low-temperature plasticity according to Mei et al. (2010) from 320 kJ/mol to 190 kJ/mol produces agreement between predicted and observed  $T_e$  (Figure 5).

### 4.3 Rheology of Subducting Lithosphere

Hunter & Watts (2016) reported that laboratory-derived rheology is consistent with subducting lithosphere based on the YSE method and the BEPM. This conclusion was based on an inversion which fit a uniform value of  $T_e$  to observed gravity profiles  $\geq 600$  km in length. However, laboratory-derived rheology is much too strong compared to Hawaiian lithosphere (Zhong & Watts, 2013; Bellas et al., 2020) and the vast majority of ocean island settings (Figure 5). This disagreement gives rise to a conundrum in which the rheology of subducting lithosphere appears stronger than that of plate interior-settings and is a major motivation of the present study.

Based on the highly uniform composition of oceanic lithosphere, we expect that subducting lithosphere at circum-Pacific subduction zones would have equivalent rheology to the lithosphere at Hawaii and other oceanic plate interior settings, barring differences associated with size effects (Kumamoto et al., 2017), strain hardening (Hansen et al., 2019), and chemical or mechanical alteration (e.g., Ranero et al., 2003; Huisman & Beaumont, 2003). At Hawaii, one of the largest ocean-island loads on Earth, flexure of  $\sim 5$  km has accumulated over  $\sim 1$  Myr (Moore & Clague, 1992) which is comparable to the amount and rate of deformation at many circum-Pacific subduction zones ( $\dot{\epsilon} \sim 10^{-16} \text{ s}^{-1}$ ). This suggests that lithospheric rheology would be similarly affected by deformation (i.e., size effects and strain hardening) at Hawaii compared to subduction zones, where the effects are likely saturated at both settings. In contrast, curvature at circum-Pacific subduction zones ( $\sim 10^{-6} \text{ m}^{-1}$ ) is significantly larger than that at Hawaii ( $\sim 10^{-7} \text{ m}^{-1}$ ) such that larger stress, greater activation of yielding mechanisms (Garcia et al., 2019), and a greater potential for chemical and mechanical alteration, are all associated with subducting

624 lithosphere. This suggests that, if anything, the rheology of subducting lithosphere should be  
625 weaker than that of the oceanic plate interior, which makes it even more difficult to reconcile  
626 why laboratory-derived rheology appears consistent with subduction zones (Hunter & Watts,  
627 2016) but it too strong compared to ocean island settings (Zhong & Watts, 2013). In other words,  
628 if laboratory-derived rheology is too strong at plate interior settings, we would expect it to be  
629 *much* too strong at subduction zones.

630 Our modeling calculations reveal that the existence of a free edge and the properties of a weak  
631 zone can significantly enhance the flexural response to a load (Figure 3d, Figure 7). This  
632 suggests that tradeoff may occur between the free edge and  $T_e$  inferred by the BEPM when it is  
633 applied to real Earth systems that do not possess an equally free edge (e.g., subducting  
634 lithosphere). Important questions arise regarding the implications of this tradeoff. For example,  
635 to what degree does tradeoff in the BEPM influence constraints on the rheology of subducting  
636 lithosphere? Unfortunately, we are presently unable to quantify the degree to which the BEPM  
637 overestimates  $T_e$  due to tradeoff with the free edge. However, because laboratory-derived  
638 rheology is too strong compared to plate interior settings, we suggest that this newly identified  
639 tradeoff may be partially responsible for the apparent agreement between laboratory-derived  
640 rheology and subducting lithosphere shown in recent studies (Hunter & Watts, 2016).  
641 Furthermore, it is essential that subducting lithosphere be weaker than the plate interior because  
642 such a variation in strength is required for the formation of trenches and subduction zones and  
643 plate-like deformation. It is not sufficient that lithospheric loads be localized at plate boundaries,  
644 because the deformational response of a uniformly high yield-stress lithosphere would be diffuse,  
645 in contrast to the intense degree of localization that is observed at plate boundaries.

The problems associated with the BEPM may be far-reaching and have broad implications for understanding lithospheric rheology and how it varies between tectonic settings. For example, most estimates of  $T_e$  at plate boundaries have been derived using the BEPM (Hanks, 1971; Parsons & Molnar, 1976; Caldwell et al. 1976; McNutt & Menard, 1982; Wessel & Haxby, 1990; Levitt & Sandwell, 1995; Hunter & Watts, 2016). It is interesting to note that the BEPM has been used in trenches and fracture zones where the isotherm to which  $T_e$  corresponds is unusually high ( $\sim 700$  °C), despite the expectation that the lithosphere be weakest at plate boundary settings. The BEPM has also been widely used to model the flexure of foreland basins which form in front of mountain belts, including the India-Eurasian collisional system (Lyon-Caen & Molnar, 1983; Karner & Watts, 1983; Jordan & Watts, 2005).

Flexure at subduction zones comprises a high degree of tectonic complexity ranging from the major thrust fault separating subducting and overriding plates, to mainly normal faults in the trench-outer-rise (Ranero & Sallarès, 2004; Ranero et al., 2003), to laterally varying  $T_e$  (Hunter & Watts, 2016), and high-stress activation of ductile yield mechanisms to the point of bending moment saturation (Garcia et al., 2019), all of which make it difficult to assess the applicability of a free edge as in the BEPM. For example, it is not clear to what degree  $T_e$  reduces as it traverses the region between the outer-rise and the trench axis and therefore to what degree the subducting lithosphere can be treated as a completely unconstrained free edge at the trench. The properties of this reduction in  $T_e$  most likely depend on the age, curvature, fault geometry at individual subduction zones, and mechanical and chemical alteration. Furthermore, it is both challenging and necessary to represent the distributed negative buoyancy force from the subducted slab in the mantle which may ultimately be responsible for the trench and outer-rise topography (e.g., Zhong & Gurnis, 1994). It is also unclear what loading effects may be

associated with arc-volcanoes which often exhibit large positive gravity anomalies and are therefore at least partially supported by lithospheric stresses (Basset & Watts, 2015). We suggest that fully dynamic viscoelastic models of subduction including internal loads from buoyancy will be required to reassess previous constraints on the rheological parameters at subduction zones. It will be highly instructive to test whether the modified rheological parameters that reproduce flexure at the Hawaiian Islands (e.g., Zhong & Watts, 2013; Bellas et al., 2020), and most oceanic plate interior flexure systems (Figure 5), also reproduce flexure at subduction zones in future studies.

At present, how to reconcile laboratory-derived rheology with flexure at subduction zones remains an open question, but low-temperature plasticity, specifically, appears to be too strong compared to oceanic lithosphere. This conclusion is also reflected in a recent study which employed models of flexure at subduction zones considering frictional, low-temperature plasticity, elastic and high-temperature creep deformation mechanisms, and produced a relatively poor fit to observations at flexure-sensitive wavelengths associated with the outer-rise at the Marianas trench (Bessat et al., 2020). We suggest that the source of the apparent disagreement may be that the rheology of low-temperature plasticity varies significantly between laboratory and lithospheric conditions, or that a multivariate modification to rheological parameters is required to improve the fit to both laboratory and field observations. Other possibilities include that low-temperature plasticity may become decreasingly relevant with grainsize reduction (Kumamoto et al., 2017), strain hardening (Hansen et al., 2019), and/or serpentinization (Chernak & Hirth, 2010), all of which likely occur at subduction zones. However, this would require a source of exorbitant weakening in the frictional sliding or high-temperature creep

deformation mechanisms to compensate for the relative strengthening in low-temperature plasticity.

## **5. Conclusions**

In this study, we first demonstrated that laboratory-derived rheology consistently overestimated a global catalogue of elastic thickness estimates at ocean island settings by a factor of two. Since this discrepancy is global and consistent, we suggest that the discrepancy cannot be explained by anomalous thermal and magmatic structures, which vary significantly between different ocean island settings, though some authors have suggested this explains the discrepancy at the Hawaiian Islands. Rather, we argue that the discrepancy is caused by laboratory-derived rheology being too strong compared to the real Earth. We have also shown that the only way to bring predictions of  $T_e$  into agreement with observations is to reduce the strength of low-temperature plasticity (e.g., by reducing the activation energy), consistent with previous work (e.g., Bellas et al., 2020). A reduction in the strength of low-temperature plasticity is required because it controls the flexural strength of the lithosphere to first order.

Second, we have verified that the yield stress envelope (YSE) method accurately reproduces  $T_e$  and stress compared to fully dynamic viscoelastic loading models (~10% error). We showed that the YSE method is only modestly sensitive to error in curvature and strain rate, though this sensitivity increases with the degree of bending. We also demonstrate the type of error that arises in the elastic plate model (EPM) when the thin plate approximation and others break down in the Appendix A for especially keen readers.

Third, we have demonstrated that the flexural response to a load is significantly enhanced when a free edge is introduced to the system. This has implications for applying the broken elastic plate model (BEPM) to real Earth systems where a completely unconstrained free edge

may not exist. Our models show that the flexural response to a load is a function of both plate strength and the properties of the free edge, such that tradeoff may occur to conserve the total elastic thickness and fit the observational data.

We propose that tradeoff between the free edge and  $T_e$  in the BEPM is partially responsible for the agreement between laboratory-derived rheology and subducting lithosphere in recent studies. This is particularly important in light of our new results, which show that laboratory-derived rheology is too strong compared to ocean island settings in genera. It will be important to re-assess the estimates of  $T_e$  and constraints on lithospheric rheology at subduction zones in future studies using models that incorporate more realistic subduction zone geometry, especially the continuity of the lithosphere, and slab buoyancy.

## Acknowledgements

We are thankful for support from NSF EAR-1940026 without which this research would not be possible. We are grateful to the two anonymous reviewers for their careful and constructive review. This work was conceptualized by A. Bellas, S. Zhong, and A. Watts, the formal analysis and visualization of results was conducted by A. Bellas, and the paper was written by A. Bellas and S. Zhong with important input from A. Watts.

## Data Availability

The 2D Cartesian viscoelastic loading model and a sample input file are available for download from: <https://doi.org/10.6084/m9.figshare.14226716>.

## References

- Bassett, D., and A. B. Watts (2015), Gravity anomalies, crustal structure, and seismicity at subduction zones: 2. Interrelationships between fore-arc structure and seismogenic behavior, *Geochem. Geophys. Geosyst.*, **16**, 1541–1576, doi:10.1002/2014GC005685
- Bellas, A., S.J. Zhong, & A.B. Watts, (2020). Constraints on the rheology of the lithosphere from flexure of the Pacific Plate at the Hawaiian Islands, *Geochemistry, Geophysics, Geosystems*, **21**, e2019GC008819. <https://doi.org/10.1029/2019GC008819>.
- Bessat, A., T. Duretz, G. Hetenyi S. Pilet & S.M. Schmalholz (2020), Stress and deformation mechanisms at a subduction zone: insights from 2-D thermomechanical numerical modelling, **221**, 1605-1625.
- Billen, M.I. & M. Gurnis, (2005). Constraints on subducting plate strength within the Kermadec trench, *J. Geophys. Res.*, **110**(B5), doi:10.1029/2004JB003308.
- Bodine, J.H., M.S. Steckler, & A.B. Watts, (1981). Observations of flexure and the rheology of the oceanic lithosphere, *J. Geophys. Res.*, **86**(B5), 3695–3707.
- Buck, W. R., L. L. Lavier, and E. Choi (2015), Magma explains low estimates of lithospheric strength based on flexure of ocean island loads, *EGU General Assembly 2015, April, Vienna, Austria*. <http://ui.adsabs.harvard.edu/abs/2015EGUGA..1714525B/abstract>.
- Burov, E.B. & M. Diament, (1995). The effective elastic thickness ( $T_e$ ) of continental lithosphere: what does it really mean?, *J. Geophys. Res.*, **100**(B3), 3905–3927.
- Byerlee, J., (1978). Friction of rocks, *Pure appl. Geophys.*, **116**(4-5), 615–626.
- Cadio, C., M.D. Ballmer, I. Panet, M. Diament, & N. Ribe (2012). New constraints on the origin of the Hawaiian swell from wavelet analysis of the geoid to topography ratio, *Earth and Planetary Science Letters*, 359-360, 40-54.
- Caldwell, J. G., W.F. Haxby, D.E. Karig, & D.L. Turcotte, (1976). On the applicability of a universal elastic trench profile, *Earth and Planetary Science Letters*, **31**(2), 239–246.
- Caldwell, J.G. & D.L. Turcotte, (1979). Dependence of the thickness of the elastic oceanic lithosphere on age, *J. Geophys. Res.*, **84**(B13), 7572–7576.
- Chernak, L.J., & G. Hirth, (2010). Deformation of antigorite serpentinite at high temperature and pressure, *Earth and Planetary Science Letters*, **296**, 23–33, doi:10.1016/j.epsl.2010.04.035.
- Contreras-Reyes, E. & A. Osses, (2010). Lithospheric flexure modelling seaward of the Chile trench: implications for oceanic plate weakening in the Trench Outer Rise region, *Geophys. J. Int.*, **182**(1), 97–112.



- 764 Craig, T.J., A. Copley & J. Jackson (2014). A reassessment of outer-rise seismicity and its  
765 implications for the mechanics of oceanic lithosphere, *Geophys. J. Int.*, **197**, 63–89.
- 766 Craig, T.J., A. Copley, & T.A. Middleton (2014). Constraining fault friction in oceanic  
767 lithosphere using the dip angles of newly-formed faults at outer rises, *Earth Planet. Sci. Lett.*,  
768 **392**, 94–99.
- 769 England, P. (2018). On shear stresses, temperatures, and the maximum magnitudes of  
770 earthquakes at convergent plate boundaries, *J. Geophys. Res.: Solid Earth*, **123**, 7165–7202.  
771 <https://doi.org/10.1029/2018JB015907>.
- 772 Escartín, J., G. Hirth, & B. Evans, (2001). Strength of slightly serpentinized peridotites:  
773 implications for the tectonics of oceanic lithosphere, *Geology*, **29**(11), 1023–1026.
- 774 Evans, B.W., H. Johannes, H. Oterdoom, V. Trommsdorff, (1976). Stability of chrysotile and  
775 antigorite in the serpentinite multisystem, *Schweiz. Mineral. Petrogr. Mitt.* **56**, 79–93.
- 776 Freed, A. M., T. Herring, and R. Bürgmann (2010). Steady-state laboratory flow laws alone fail  
777 to explain post-seismic observations, *Earth Planet. Sci. Lett.*, **300**, 1–10.
- 778 Gao, X., & K. Wang (2014). Strength of stick-slip and creeping subduction megathrusts from  
779 heat flow observations, *Science*, **345**, 1038–1041.
- 780 Garcia, E.S.M., D. T. Sandwell & D. Bassett (2019). Outer trench slope flexure and faulting at  
781 Pacific basin subduction zones, *Geophys. J. Int.* **218**, 708–728.
- 782 Goetze, C. & B. Evans, (1979). Stress and temperature in the bending lithosphere as constrained  
783 by experimental rock mechanics, *Geophys. J. Int.*, **59**(3), 463–478.
- 784 Goetze, C., and B. Evans (1979), Stress and temperature in the bending lithosphere as constrained by  
785 experimental rock mechanics, *Geophys. J. R. Astr. Soc.*, **59**, 463–478.
- 786 Griggs D.T., & J.D. Blacic, (1965). Quartz: Anomalous Weakness of Synthetic Crystals, *Science*,  
787 **147**(15), 3655, 292–295, DOI: 10.1126/science.147.3655.292.
- 788 Guest, I., G. Ito, M.O. Garcia, & E. Hellebrand (2020). Extensive magmatic heating of the  
789 lithosphere beneath the Hawaiian Islands inferred from Salt Lake Crater Mantle xenoliths,  
790 *Geochemistry, Geophysics, Geosystems*, **21**, e2020GC009359. <https://doi.org/10.1029/2020GC009359>
- 792 Hager, B. H., & M. A. Richards (1989). Long-wavelength variations in Earth's geoid: Physical  
793 models and dynamical implications, *Philos. Trans. R. Soc. London, Ser. A*, **328**, 309–327.

- 794 Hanks, T. C., (1971). The Kuril Trench-Hokkaido Rise System: Large Shallow Earthquakes and  
 795 Simple Models of Deformation, *Geophysical Journal of the Royal Astronomical Society*, 23(2),  
 796 173–189.
- 797 Hansen L.N., E.C. David, N. Brantut, & D. Wallis, (2020). Insight into the microphysics of  
 798 antigorite deformation from spherical nanoindentation, *Phil. Trans. R. Soc. A* **378**: 20190197,  
 799 <http://dx.doi.org/10.1098/rsta.2019.01979>.
- 800 Hansen, L.N., K.M. Kumamoto, C.A. Thom, D. Wallis, W.B. Durham, & D.L. Goldsby, (2019).  
 801 Low-temperature plasticity in olivine: Grain size, strain hardening, and the strength of the  
 802 lithosphere, *J. Geophys. Res.*, 124, 5427–5449, <https://doi.org/10.1029/2018JB016736>.
- 803 Hirano, N., A. A. P. Koppers, A. Takahashi, T. Fujiwara, and M. Nakanishi (2008), Seamounts, knolls  
 804 and petit-spot monogenetic volcanoes on the subducting Pacific plate, *Basin Research*,  
 805 doi:10.1111/j.1365-2008.00363.x, 1-11.
- 806 Hirth, G., & D. L. Kohlstedt (2003), Rheology of the upper mantle and the mantle wedge: A  
 807 view from the experimentalists, in *Inside the Subduction Factory*, Geophysical Monograph, vol.  
 808 138, edited by J. Eiler, pp. 83–105, AGU, Washington, D. C.
- 809 Huismans, R. S., & C. Beaumont, (2003). Symmetric and asymmetric lithospheric extension:  
 810 Relative effects of frictional-plastic and viscous strain softening, *J. Geophys. Res.*, **108**, B10,  
 811 2496, doi:10.1029/2002JB002026.
- 812 Hunter, J., & A.B. Watts, (2016). Gravity anomalies, flexure, and mantle rheology seaward of  
 813 circum-Pacific trenches, *Geophys. J. Int.* **207**, 288–316.
- 814 Jain, C., J. Korenaga, & S.-I. Karato, (2017). On the yield strength of oceanic lithosphere,  
 815 *Geophysical Research Letters*, 44, 9716–9722, <https://doi.org/10.1002/2017GL075043>.
- 816 Karato, S.I. (2012). Rheological Properties of Minerals and Rocks, *Physics and Chemistry of the*  
 817 *Deep Earth*, Wiley-Blackwell.
- 818 Karato, S.-I., & P. Wu (1993), Rheology of the upper mantle, *Science*, 260, 771–778.
- 819 Karner, G.D. & A.B. Watts (1983). Gravity anomalies and flexure of the lithosphere at mountain  
 820 ranges, *J. Geophys. Res.*, **88(B12)**, 10449-10477.
- 821 Kumamoto, K.M., C.A. Thom, D. Wallis, L.N. Hansen, D.E.J. Armstrong, & J.M. Warren,  
 822 (2017). Size effects resolve discrepancies in 40 years of work on low-temperature plasticity in  
 823 olivine, *Science Advances*, 3(9), e1701338, <https://doi.org/10.1126/sciadv.1701338>.
- 824 Levitt D.A. & D.T. Sandwell, (1995). Lithospheric bending at subduction zones based on depth  
 825 soundings and satellite gravity, *J. Geophys. Res.*, **100(B1)**, 379-400.

- 826 Lyon-Caen, H., & P. Molnar (1983). Constraints on the structure of the Himalaya from an  
827 analysis of gravity anomalies and a flexural model of the lithosphere, *J. Geophys. Res.*, **88**(B10),  
828 8171-8191.
- 829 McAdoo, D.C., & C.F. Martin, (1984). Seasat observations of lithospheric flexure seaward of  
830 trenches, *J. Geophys. Res.*, **89**(B5), 3201-3210.
- 831 McAdoo, D.C., J.G. Caldwell, & D.L. Turcotte, (1978). On the elastic perfectly plastic bending  
832 of the lithosphere under generalized loading with application to the Kuril Trench, *Geophys. J.*  
833 *Int.*, **54**(1), 11–26.
- 834 McNutt, M. (1984). Lithospheric flexure and thermal anomalies, *J. Geophys. Res.*, **89**(B13),  
835 11,180-11,194.
- 836 McNutt, M.K. & H.W. Menard, (1982). Constraints on yield strength in the oceanic lithosphere  
837 derived from observations of flexure, *Geophys. J. Int.*, **71**(2), 363–394.
- 838 Mei, S., A.M. Suzuki, D.L. Kohlstedt, N.A. Dixon, & W.B. Durham, (2010). Experimental  
839 constraints on the strength of the lithospheric mantle, *J. Geophys. Res.*, **115**(B8),  
840 doi:10.1029/2009JB006873.
- 841 Mitrovica, J., & A. M. Forte (1997), Radial profile of mantle viscosity: results from the joint  
842 inversion of convection and postglacial rebound observables, *J. Geophys. Res.*, **102**, 2751–2769.
- 843 Moore, J. G., & D. A. Clague (1992), Volcano growth and evolution of the island of Hawaii,  
844 *Geol. Soc. Am. Bull.*, **104**, 1471–1484.
- 845 Mueller, S. & R.J. Phillips, (1995). On the reliability of lithospheric constraints derived from  
846 models of outer-rise flexure, *Geophys. J. Int.*, **123**(3), 887–902.
- 847 Parsons, B. & P. Molnar, (1976). The Origin of Outer Topographic Rises Associated with  
848 Trenches, *Geophys. J. Int.*, **1**(4), 707–712.
- 849 Pleus, A., G. Ito, P. Wessel, & L.N. Frazer, (2020). Rheology and thermal structure of the  
850 lithosphere beneath the Hawaiian Ridge inferred from gravity data and models of plate flexure,  
851 *Geophys. J. Int.* **222**, 207–224.
- 852 Podolefsky, N.S., S.J. Zhong, & A.K. McNamara, (2004). The anisotropic and rheological  
853 structure of the oceanic upper mantle from a simple model of plate shear, *Geophys. J. Int.*, **158**,  
854 287–296.
- 855 Ranero, C.R. & V. Sallarès, (2004). Geophysical evidence for hydration of the crust and mantle  
856 of the Nazca plate during bending at the north Chile trench, *Geology*, **32**(7), 549–552

- 857 Ranero, C.R., Morgan, J.P., McIntosh, K., Reichert, C. (2003), Bending-related faulting and  
858 mantle serpentinization at the Middle America trench, *Nature*, 425, 367-373.
- 859 Reinen, L.A., J.D. Weeks, & T.E. Tullis, (1994). The frictional behavior of lizardite and  
860 antigorite serpentinites: Experiments, constitutive models, and implications for natural  
861 faults, *PAGEOPH* **143**, 317–358, <https://doi.org/10.1007/BF00874334>.
- 862 Reuber, G.S., L. Holbach, A.A. Popov, M. Hanke, & B.J.P. Kaus (2020). Inferring rheology and  
863 geometry of subsurface structures by adjoint-based inversion of principal stress directions,  
864 *Geophys. J. Int.*, **223**-2, 851-861, <https://doi.org/10.1093/gji/ggaa344>
- 865 Ribe, N. M., & U.R. Christensen, (1994). 3-Dimensional modeling of plume-lithosphere  
866 interaction, *J. Geophys. Res.*, 99, 669–682.
- 867 Sandwell, D. & G. Schubert, (1980). Geoid height versus age for symmetric spreading ridges, *J.*  
868 *Geophys. Res.*, **85**(B12), 7235–7241.
- 869 Sibson, R.H. (1974). Frictional constraints on thrust, wrench and normal faults, *Nature*, **249**,  
870 542-544.
- 871 Smith, W.H.F., H. Staudigel, A.B. Watts, & M.S. Pringle (1989), The Magellan Seamounts:  
872 Early Cretaceous Record of the South Pacific Isotopic and Thermal Anomaly, *J. Geophys. Res.*,  
873 **94**(B8), 10,501-10-523.
- 874 Turcotte, D.L. & G. Schubert, (1982). *Geodynamics: Applications of Continuum Physics to*  
875 *Geological Problems*, John Wiley & Sons, 450 pp.
- 876 Turcotte, D.L., D.C. McAdoo, & J.G. Caldwell, (1978). An elastic-perfectly plastic analysis of  
877 the bending of the lithosphere at a trench, *Tectonophysics*, **47**(3), 193–205.
- 878 Von Herzen, R.P., M.J. Cordery, R.S. Detrick, & C. Fang, (1989). Heat flow and the thermal  
879 origin of hot spot swells: the Hawaiian swell revisited, *J. geophys. Res.*, **94**(B10), 13 783–13 799.
- 880 Walcott, R., (1970). Flexural Rigidity, Thickness, and Viscosity of the Lithosphere, *J. geophys.*  
881 *Res.*, 75(20), 3941–3954.
- 882 Watts, A. B., & U.S. ten Brink (1989). Crustal structure, flexure, and subsidence history of the  
883 Hawaiian Islands, *J. Geophys. Res.*, 94, 10,473-10,500.
- 884 Watts, A. B., and E. B. Burov (2003), Lithospheric strength and its relationship to the elastic and  
885 seismogenic layer thickness, *Earth and Planetary Science Letters*, 213, 113-131, doi:10.1016/S0012-  
886 821X(03)00289-9.

- 887 Watts, A.B. & M. Talwani (1974). Gravity Anomalies Seaward of Deep-Sea Trenches and their  
888 Tectonic Implications, *Geophys. J. Int.*, **36**(1), 57–90.
- 889 Watts, A. B., Grevemeyer, I., Shillington, D. J., Dunn, R. A., Boston, B., & Gomez de la Pena, L.  
890 (2021). Seismic structure, gravity anomalies and flexure along the Emperor Seamount chain. *J.*  
891 *Geophys. Res.: Solid Earth*, **126**, e2020JB021109. <https://doi.org/10.1029/2020JB021109>
- 892 Watts, A.B., (2001). *Isostasy and Flexure of the Lithosphere*, Cambridge Univ. Press.
- 893 Wessel, P. (1993). A Reexamination of the Flexural Deformation Beneath the Hawaiian Islands,  
894 *J. Geophys. Res.*, **98**, 12177-12190.
- 895 Wessel, P., & W. Haxby (1990). Thermal stresses different subsidence, and flexure and oceanic  
896 fracture zones, *J. Geophys. Res.*, **95**(B1), 375-391.
- 897 Zhong, S.J. & A.B. Watts (2002). Constraints on the dynamics of mantle plumes from uplift of  
898 the Hawaiian Islands, *Earth Planet. Sci. Lett.*, **203** 105-116.
- 899 Zhong, S. J. & A.B. Watts, (2013). Lithospheric deformation induced by loading of the Hawaiian  
900 Islands and its implications for mantle rheology, *J. Geophys. Res.*, **118**(11), 6025–6048.
- 901 Zhong, S. J. & M. Gurnis (1994). Controls on trench topography from dynamic models of  
902 subducted slabs, *J. Geophys. Res.*, **99**(B8), 15,683–15,695.
- 903 Zhong, S. J. (1997). Dynamics of crustal compensation and its influences on crustal isostasy, *J.*  
904 *Geophys. Res.*, **102**, 15,287–15,299.
- 905 Zhong, S. J., A. Paulson, & J. Wahr (2003). Three-dimensional finite element modeling of  
906 Earth's viscoelastic deformation: Effects of lateral variations in lithospheric thickness, *Geophys.*  
907 *J. Int.*, **155**, 679–695.
- 908 Zoback, M. D., & J. Townend, (2001). Implications of hydrostatic pore pressures and high  
909 crustal strength for the deformation of intraplate lithosphere, *Tectonophysics*, **336**, 19–30.
- 910

## Appendix

In this appendix, we investigate the type of error that arises in the elastic plate model (EPM) when the thin plate approximation becomes decreasingly valid. This occurs when the wavelength of the load becomes comparable to the thickness of the plate (i.e.,  $\lambda \gg T_e$  becomes invalid). This is accomplished by comparing predictions from the EPM with the fully dynamic viscoelastic loading model which does not depend on the thin plate approximation (section 2.3 in the main text).

The model domain is 1500 km wide ( $x$ ) and 600 km deep ( $z$ ), and the surface load is expressed as a sinusoidal function of horizontal position  $x$

$\sigma_0(x) = \rho g A_0 \cos\left(\frac{2\pi x}{\lambda}\right)$ , in which  $\rho$  is the mantle density. For all models in the Appendix,

$A_0 = 3$  km is the load amplitude, the load is constant in time, and the viscosity structure is two-

layer with a high-viscosity layer thickness of 50 km (Figure A1). All other model parameters are

given in Table 1.

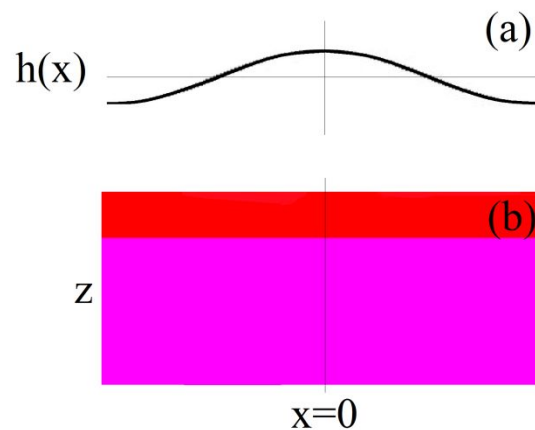


**Figure A1. Model Schematic.** The models in this Appendix are identical to those in the main text, except for the load which is sinusoidal. We consider only two-layer models in this section, and models are symmetric across  $x=0$ .

924 In Case 0a, the wavelength of the load  $\lambda=3000$  km which is much larger than  $T_e=50$  km.  
 925 Therefore, Case 0a will serve as a reference model in which we expect excellent agreement  
 926 between the fully dynamic model and the EPM. The time-dependent deformational response is  
 927 computed for 1000 time-steps or 250 Maxwell times based on mantle viscosity ( $\tau_M=\eta_0/\mu\sim 950$   
 928 years). The evolution of surface flexure and stress are shown at  $t=0$  (Figure A2a-b),  $t=12.5\tau_M$   
 929 (Figure A2c-d), and  $t=250\tau_M$  (Figure A2e-f).

930 At  $t=0$ , the deformational response is purely elastic, and the amplitude of surface flexure is  
 931  $<500$  m. After  $12.5\tau_M$ , the amplitude of surface deflection has increased to  $>2000$  m, stresses up  
 932 to 100 MPa begin to concentrate in the lithosphere, and strain rates of  $10^{-15}$  s $^{-1}$  begin to  
 933 concentrate in the weak underlying mantle. After  $250\tau_M$ , the surface flexure is sinusoidal with  
 934 amplitude  $w_0=2997.7$  m which almost fully compensates the surface load (Figure A2e), stresses  
 935 in the weak underlying mantle have fully relaxed (Figure A2f), and the system is in steady state.  
 936 Stresses in the lithosphere decrease between  $12.5\tau_M$  and  $250\tau_M$  possibly because the load  
 937 becomes almost fully compensated such that the forcing from a horizontal gradient in  
 938 topography is removed. Near-complete compensation of a long-wavelength load is consistent  
 939 with analytical solutions of viscoelastic loading (e.g., Zhong, 1997).

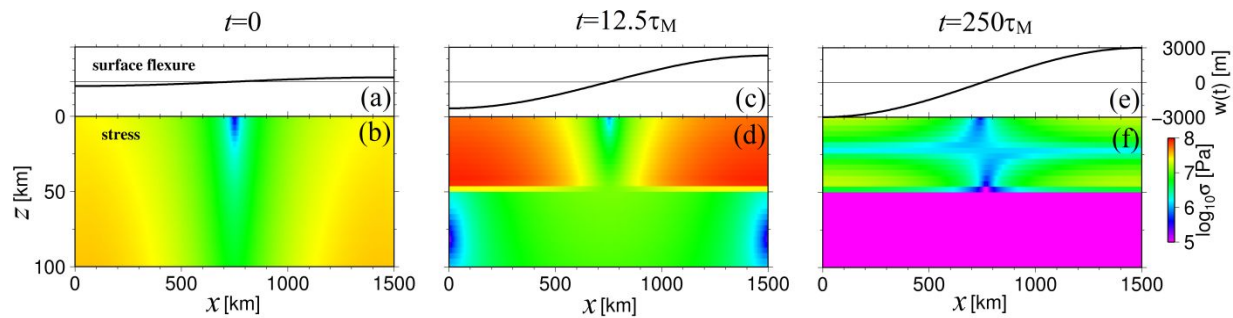


**Figure A2. Time evolution of two-layer viscosity model Case 0a.** The surface deflection and the stress field for varying time in response to a sinusoidal load. At  $t=0$  (a-b), the response is entirely elastic such that stress is distributed relatively evenly in depth. At  $t=12.5\tau_M$  (c-d), viscous relaxation causes stress to concentrate in the high viscosity layer. At  $t=250\tau_M$  (e-f), the system is in steady state, elastic stresses are concentrated in the high viscosity layer, and the flexure is maximal.

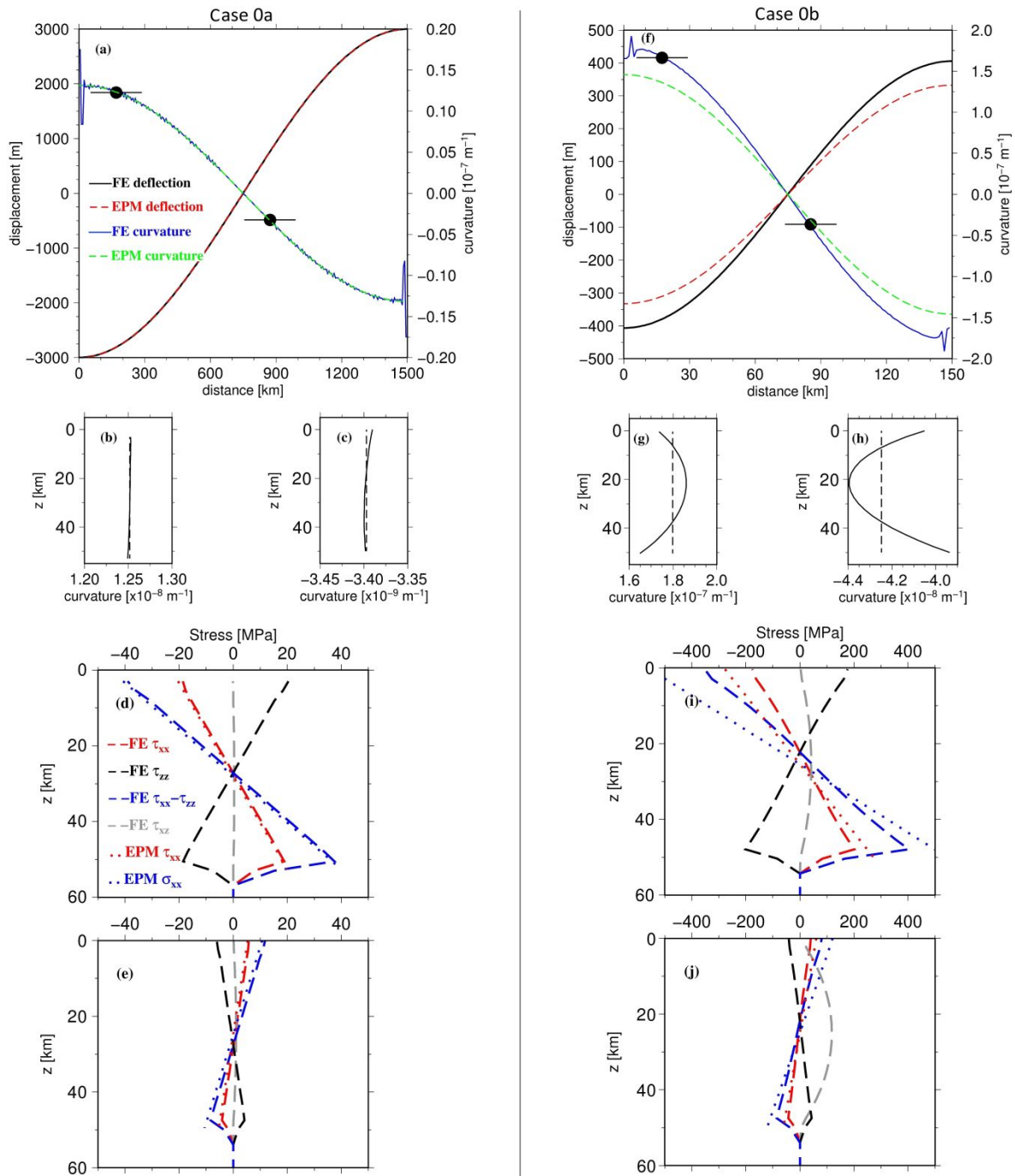


**Figure A3. Comparison of predictions from the elastic plate model and the fully dynamic model.** In the left column (a-e) are results from Case 0a which is subject to a 3000 km wavelength load. On the right (f-j) are results from Case 0b which is subject to a 300 km wavelength load. From top to bottom, we present the surface deflection and surface curvature (a, f); (solid) the internal or depth-dependent curvature which is horizontally averaged over the ranges (bars) centered on circles in (a) and (f), and (dashed) the vertical average (b-c, g-h);



(dashed) the numerical or finite element (FE) vertical stress profiles averaged near the domain edge marked by leftmost circles in (a) and (f), and (dotted) the elastic plate model (EPM) prediction (d, i); finally, (dashed) the numerical (FE) vertical stress profiles averaged near the domain center marked by central circles in (a) and (f), and (dotted) the EPM prediction (e, j). In the legend for stress profiles,  $\tau$  represents deviatoric stress, and  $\sigma$  represents total stress.

The flexure of Case 0a agrees almost identically with the prediction from the EPM for  $T_e=50$  km and the same load (Turcotte and Schubert, 1982), which also predicts a sinusoidal surface displacement with the same amplitude of  $w_0=2997.6$  m for the elastic plate parameters used here (Figure A3a). The curvature from both models is also sinusoidal with amplitude  $1.31 \times 10^{-8} \text{ m}^{-1}$  and in good agreement with each other. Note that the curvature predicted by the EPM is expressed  $\kappa=d^2w/dx^2=w_0(2\pi/\lambda)^2$  (Figure A3a). Numerical error at the domain boundaries is associated with computing the second order derivative of displacement which is less accurate than the displacement itself.

In Case 0a, it is also possible to investigate internal or depth-dependent curvature within the lithosphere although curvature is treated as constant in depth in the EPM (Figure A3b-c). Curvature from Case 0a is constant in depth near the domain edge as well as near the domain center (Figure A3b and Figure A3c for horizontally averaged curvatures at  $x=50\text{-}300$  km and  $x=750\text{-}1000$  km, respectively, marked by circles in Figure A3a). Constant curvature with respect to depth affirms that variations in depth are negligible for long-wavelength loads compared to plate thickness, consistent with the thin plate approximation and the EPM.

The stress from Case 0a is compared with stress predicted by the EPM at the same two locations where curvature is averaged (i.e., Figure A3d and A3e for horizontally averaged between  $x=50\text{-}300$  km and  $x=750\text{-}1000$  km, respectively). For Case 0a, the deviatoric normal stresses are equal and opposite ( $\tau_{xx}=-\tau_{zz}$ ), the deviatoric shear stress is small ( $\tau_{xz}\sim 0$ ), and the differential stress is twice the deviatoric normal stress ( $\tau_{xx}-\tau_{zz}=2\tau_{xx}$ ) (Figure A3d-e), as expected for an incompressible medium with  $du_x/dx=-du_z/dz$  (i.e., equation 7) and constant viscosity. The EPM prediction  $\sigma_{xx}$  agrees well with the differential stress from Case 0a  $\tau_{xx}-\tau_{zz}$  because the thin plate approximation assumes  $\sigma_{zz}=0$  at the surface and throughout the plate, such that  $\sigma_{xx}$  is equal

to the differential stress (i.e.,  $\sigma_{xx} = \sigma_{xx} - \sigma_{zz} = \tau_{xx} - \tau_{zz}$ ). Note that  $\sigma_{xx}$  from the EPM is a total stress component (i.e., including the hydrostatic component), whereas our numerical model predicts deviatoric stresses.

The deviatoric components of stress based on the EPM are derived in the following to show they also agree with those in the fully dynamic model (Figure A3d-e). The hydrostatic component of stress in the EPM is expressed  $-P = 1/3(\sigma_{xx} + \sigma_{yy} + \sigma_{zz})$  which can be rewritten -  $P = \sigma_{xx}(1 + \nu)/3$  since  $\nu\sigma_{yy} = \sigma_{xx}$  and  $\sigma_{zz} = 0$  (Turcotte and Schubert, 1982). Removing the hydrostatic component from the total stresses produces the deviatoric stress components according to the EPM,

$$\tau_{xx} = \frac{2 - \nu}{3} \sigma_{xx} \quad \#(A2)$$

$$\tau_{zz} = -\frac{2 - \nu}{3} \sigma_{xx} \quad \#(A3)$$

$$\tau_{yy} = \frac{2\nu - 1}{3} \sigma_{xx} \quad \#(A4)$$

Since incompressibility is imposed in the numerical models, we let  $\nu = 0.5$  in the EPM as well. It is worth noting that while incompressibility is equivalent to  $\nu = 0.5$ , most crustal and mantle rocks are Poisson solids, for which  $\nu \sim 0.3$ , but we do not expect this difference to significantly alter the results. The deviatoric stress components from the EPM are thus  $\tau_{xx} = \sigma_{xx}/2$ ,  $\tau_{zz} = -\sigma_{xx}/2$ , and  $\tau_{yy} = 0$ , all of which are identical to the fully dynamic numerical solutions (Figure A3d-e). Finally, we note that the total stress  $\sigma_{xx}$  and not the deviatoric normal stress  $\tau_{xx}$  should be integrated to solve the bending moment because all forces related to bending are encapsulated in  $\sigma_{xx}$  but not  $\tau_{xx}$  (equation 4 or equation 6).

Next, in Case 0b, we investigate the type of error that arises in the EPM for a load wavelength comparable to the plate thickness. The wavelength of the load is reduced by a factor of 10 relative to Case 0a such that  $\lambda = 300$  km, the horizontal model domain is reduced to 150 km, and all other aspects of Case 0a and 0b are identical. The surface flexure and curvature are sinusoidal with amplitudes 406.6 m and  $1.75 \times 10^{-7} \text{ m}^{-1}$ , respectively (Figure A3f). Internal curvature of the lithosphere varies appreciably with depth in contrast to Case 0a, both near the domain edge at  $x = 5$ -30 km (Figure A3g) and near the domain center at  $x = 75$ -100 km (Figure A3h). We also note that the depth-averaged internal curvature is greater in magnitude than the surface curvature

regardless of whether the flexure is concave-up (Figure A3g) or concave-down (Figure A3h). We suggest that vertical variation of curvature within the plate may be one manifestation of the breakdown of the thin plate approximation. Stresses are approximately an order of magnitude larger compared with Case 0a, and the shear stress  $\tau_{xz}$  increases especially at mid-plate depths (Figure A3i-j).

In comparison, the EPM predicts the amplitudes of deflection and curvature are 332.4 m and  $1.46 \times 10^{-7} \text{ m}^{-1}$ , both of which are underestimates compared to the numerical results (Figure A3f) and overestimates the differential stress (Figure A3i-j). If we consider the fact that the EPM overestimates the numerical stress based on the surface curvature taken from the numerical Case 0b, which is smaller in magnitude at the surface than the plate interior, then this demonstrates that vertical variations in curvature are not the only manifestation of thick plate effects, because curvature smaller than the depth-averaged value alone would cause the EPM to underestimate elastic bending stresses. Therefore, we show that at short-wavelengths, breakdown of the thin plate approximation is manifested in the EPM by overestimation of bending stresses in addition to underestimation of surface flexure and curvature. Understanding the type of error that arises when the thin plate approximation breaks down may help to inform the kind of limits that may be placed on short-wavelength deformation in the EPM in future studies.

In summary, we have shown that the EPM predicts flexure, curvature, and stress identical to that in fully dynamic viscoelastic loading models when the thin plate approximation and others are valid. However, the agreement degrades as the thin plate approximation breaks down, as is expected, and the disagreement is such that the EPM underestimates flexure and curvature, but overestimates stress relative to the fully dynamic numerical model. The thin plate approximation is the assertion that the depth to the neutral surface is fixed, does not vary, that no vertical variations in stress ( $\sigma_{zz}$ ,  $\sigma_{xz}$ ) or curvature ( $\kappa$ ) occur in the bending lithosphere, and the EPM relies on it and other assumptions such as small curvature and small angle approximations. It is not straightforward to identify which approximation leads to the error we observe in this study, or why the error has the sign configuration observed herein. However, understanding the behavior that arises when the approximations become decreasingly valid may help inform the limits that can be placed on flexural dynamics (i.e., upper and lower bounds on flexure, stress, curvature) in future studies which use the EPM.